

Velocity-resolved [O I] 63,145 μm , [C II] 158 μm , and OH line mapping along the Orion BN/KL explosive outflow and irradiated shocks^{*}

Javier R. Goicoechea¹, Rolf Güsten², Benjamin Godard^{3,4}, Helmut Wiesemeyer², Ronan Higgins⁵, Antoine Gusdorf^{4,3}, Miriam G. Santa-Maria¹, Marion Zannese¹, and Karl M. Menten²

¹ Instituto de Física Fundamental (CSIC). Calle Serrano 121-123, 28006, Madrid, Spain. e-mail: javier.r.goicoechea@csic.es

² Max-Planck Institut für Radioastronomie, Auf dem Hügel 69, 53121 Bonn, Germany

³ Observatoire de Paris, Université PSL, Sorbonne Université, LUX, 75014 Paris, France

⁴ Ecole Normale Supérieure, ENS, Université PSL, CNRS, Sorbonne Université, Université de Paris, 75005 Paris, France

⁵ Physikalisches Institut der Universität zu Köln, Zùlpicher Straße 77, 50937 Köln, Germany

Received 9 January 2026 / Accepted 15 May 2026

ABSTRACT

Stellar mergers produce “explosive outflows” that serve as transient sources of infrared line luminosity and inject mechanical energy early into the natal molecular cloud. We present the first velocity-resolved, sub- km s^{-1} resolution maps of the [O I] 63 and 145 μm fine-structure line emission from the wide-angle outflow in Orion BN/KL, the nearest explosive outflow. The data were obtained with the GREAT receivers on board SOFIA and include new, sensitive [C II] 158 μm and OH maps. They allowed us to disentangle the quiescent cloud gas, traced by a narrow [O I] component with a full width at half maximum (FWHM) of $\approx 4 \text{ km s}^{-1}$, from the outflow, traced by a broader [O I] component with a line FWHM of about $\approx 20\text{--}30 \text{ km s}^{-1}$; the latter exhibits a spatial distribution similar to that of the shock-excited H_2 emission seen with JWST. The [O I] 63 μm line displays a full width at zero intensity (FWZI) of $\sim 85 \text{ km s}^{-1}$ and shows foreground narrow absorptions against strong continuum sources. The OH 119 μm line shows a prominent P-Cygni profile covering $\sim 160 \text{ km s}^{-1}$, similar to the very broad FWZI of the CO lines. The total [O I] 63 and 145 μm line luminosity is remarkably high, $86.5 L_{\odot}$, of which $55 L_{\odot}$ is emitted in the broad component. This luminosity is comparable to the H_2 and CO line luminosities, implying an outflow mass-loss rate of $\dot{M} \approx (9.1 \pm 2.6) \times 10^{-3} M_{\odot} \text{ yr}^{-1}$ and a mass $M \approx (3.3\text{--}5.9) M_{\odot}$. The [O I] 63/145 and [O I] 63/[C II] 158 intensity ratios reach very high values in the line wings (20–30 and 40–60, respectively), exceeding those found in photodissociation regions. These ratios are consistent with the presence of dense ($n_{\text{H}} \approx 10^5$ to 10^6 cm^{-3}) and warm ($T \lesssim 500 \text{ K}$) postshock gas. We analyzed the fine-structure line-wing intensities using magnetized shock models that include UV irradiation, to which the [C II] 158 μm line intensity is particularly sensitive. We find that the [O I] and [C II] intensities are consistent with emission from dissociative J -type shocks with velocities of $30\text{--}40 \text{ km s}^{-1}$ and preshock gas densities of a few 10^4 cm^{-3} , illuminated by external UV radiation generated by surrounding fast shocks and possibly by massive (proto)stars in the region. We also report a broad [O I] 63 μm emission feature around the BN star, which we attribute to an unresolved outflow or wind bow shock.

Key words. Infrared: ISM – ISM: jets and outflows – shock waves – stars: protostars

1. Introduction

Explosive events triggered by mergers of protostars generate transitory infrared (IR) line luminosity bursts and inject substantial mechanical energy ($\sim 10^{47\text{--}48} \text{ erg}$) into the natal molecular cloud, serving as an early source of mechanical feedback in clustered star-forming regions (e.g., Bally & Zinnecker 2005). The resulting bow-shock tips, or “bullets”, propagate through the cloud, generating shocks that cool via molecular and atomic line emission, depending on their velocity, magnetic field, gas density, and ambient ultraviolet (UV) radiation. Stellar mergers must occur relatively frequently in clustered star-forming regions—perhaps once per century in our Galaxy (e.g., Zapata et al. 2020, 2023)—and are therefore likely to be common in luminous galaxies. The Orion BN/KL outflow (e.g., Kwan & Scoville 1976; Beckwith et al. 1978; Snell et al. 1984) is the nearest example of an “explosive outflow” (e.g., Gómez et al. 2005; Zapata et al. 2009; Goddi et al. 2011; Bally et al. 2011, 2020).

Its distinctive kinematics and diverse gas cooling lines (atomic, H_2 , CO, H_2O , and OH; e.g., Werner et al. 1984; Rosenthal et al. 2000; González-Alfonso et al. 2002; Zapata et al. 2009; Peng et al. 2012; Goicoechea et al. 2015a) indicate the presence of shocks, in which the mechanical energy of the explosion is converted into gas heating and compression as the outflow impacts the swept-up gas and the ambient molecular cloud. However, the nature of these shock(s)—“jump” (J -type), “continuous” (C -type) or mixed—as well as the role of UV radiation, whether shock-generated or external, remain uncertain. On the one hand, UV-irradiated shocks are best traced by velocity-resolved observations of the [O I] 63 and 145 μm and [C II] 158 μm cooling lines, but only a few sources have been mapped in the wings of all three lines. In particular, the scarcity of [O I] 145 μm data limits constraints on the physical conditions of the [O I]-emitting gas across velocities. On the other hand, only recently have shock models (e.g., Hollenbach & McKee 1979, 1989; Draine 1980; Kaufman & Neufeld 1996) included realistic descriptions of UV-irradiated shocks (Lesaffre et al. 2013; Melnick & Kaufman 2015; Godard et al. 2019, 2024; Lehmann et al. 2020, 2022; Kristensen et al. 2023).

^{*} Dedicated to the memory of Karl M. Menten (1957–2024), whose support for the GREAT developments and whose interest in Orion inspired these observations.

Here, we present the highest so far angular resolution [O I] 63 and 145 μm maps of the BN/KL outflow (6'' and 13'', respectively) carried out at sub- km s^{-1} resolution and complemented by sensitive line maps of [C II] 158 μm , a tracer of UV radiation and stellar feedback (e.g., [Tielens & Hollenbach 1985](#); [Stacey et al. 1993](#); [Goicoechea et al. 2015b](#); [Pabst et al. 2019](#)), and OH, a tracer of the outflow kinematics (e.g., [Melnick et al. 1987, 1990](#); [Goicoechea et al. 2006a, 2015a](#)). We obtained these observations with the *Stratospheric Observatory for Infrared Astronomy* (SOFIA; [Young et al. 2012](#)) using GREAT¹, providing a legacy dataset for studying the properties of shocked gas.

The paper is organized as follows. In Sect. 2, we provide specific details on the BN/KL outflow. In Sect. 3, we describe the airborne observations. Sect. 4 presents the main observational findings, while Sect. 5 extracts physical conditions as a function of velocity in the outflow. Finally, Sect. 6 discusses the nature of the [O I]-emitting shocks based on comparisons with state-of-the-art shock models, and places our results in the context of FIR line emission from other massive star-forming regions.

2. The Orion BN/KL explosive outflow

Embedded in the heart of the Orion Molecular Cloud-1 core (OMC-1), just behind the Orion Nebula (M42), the Becklin–Neugebauer/Kleinmann–Low (BN/KL) region is the closest (~ 414 pc; [Menten et al. 2007](#)) high-mass star-forming region ([Genzel & Stutzki 1989](#); [O’Dell 2001](#); [Bally 2008](#)). In addition to the two well-known runaway stars BN and source *I*, the most massive objects in this region (e.g., [Lonsdale et al. 1982](#); [Scoville et al. 1983](#); [Menten & Reid 1995](#); [Bally et al. 2020](#)), the field hosts the first identified molecular outflow, exhibiting high-velocity CO emission, with line wings extending to over ± 100 km s^{-1} , together with a wide-angle, shock-excited H₂ outflow (e.g., [Kwan & Scoville 1976](#); [Beckwith et al. 1978](#); [Snell et al. 1984](#)). Observations of this outflow have long provided key benchmarks for the development of shock models ([Draine & Roberge 1982](#); [Neufeld & Dalgarno 1989](#); [Hollenbach & McKee 1989](#)). Today we know that this is an explosive outflow produced by a dynamical decay event (e.g., a stellar merger), which triggered the acceleration of BN and source *I*, about 500 yr ago (e.g., [Gómez et al. 2005](#); [Zapata et al. 2009](#); [Bally et al. 2011](#); [Goddi et al. 2011](#); [Bally et al. 2020](#)). The center of the explosion is located between the current positions of these stars.

ALMA CO observations reveal an approximately spherically symmetric “Hubble-Lemaître flow”, that is, radial velocities scaling with the projected distance from the center. The flow is composed of over a hundred narrow bow-shock wakes, or “fingers”, within $\sim 1'$ (~ 0.1 pc) of the center ([Bally et al. 2017](#)). Due to the isotropic distribution of the flow, the red- and blueshifted fingers appear to overlap when projected onto the plane of the sky, a characteristic of explosive outflows. The bullets show shock-excited H₂ $v = 1-0 S(1)$ (2.12 μm) and forbidden [Fe II] 1.64 μm emission at their tips, together with H₂ and lower-velocity CO emission in their wakes (e.g., [Zapata et al. 2009](#); [Kristensen et al. 2007, 2008](#); [Nissen et al. 2012](#); [Bally et al. 2015](#); [Youngblood et al. 2018](#)). The H₂ emission shows a two-lobe northwest–southeast (NW–SE) orientation (e.g., [Allen & Burton 1993](#); [McCaughrean & Mac Low 1997](#)), likely because the other part of the outflow—or its IR emission—is partially obscured by the dense dust ridge along OMC-1, which extends toward the northeast (NE). According to

¹ The German REceiver for Astronomy at Terahertz frequencies was developed by the MPI für Radioastronomie and the KOSMA/Universität zu Köln, in cooperation with the DLR Institut für Optische Sensorsysteme.

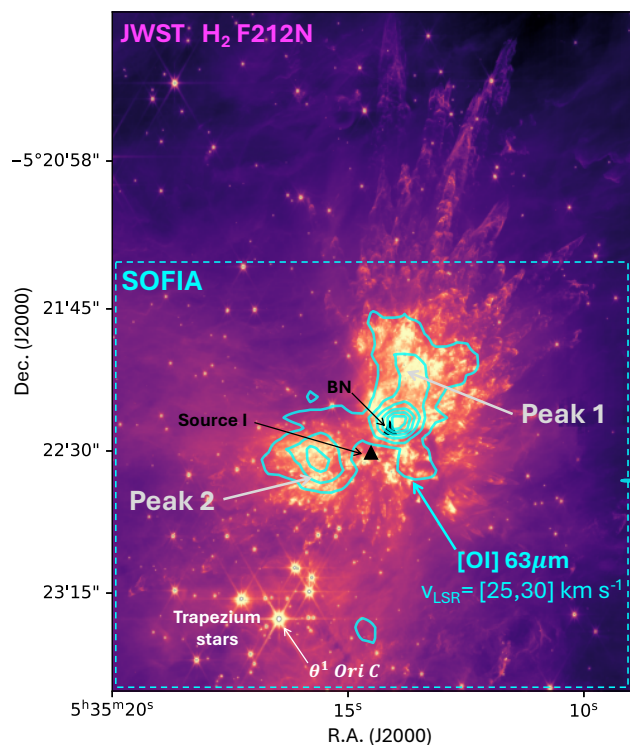


Fig. 1. BN/KL outflow and the Trapezium cluster observed with JWST/NIRCam H₂ F212N ([McCaughrean & Pearson 2023](#)). The dashed square marks the field of view mapped with SOFIA/GREAT. Cyan contours show the [O I] 63 μm redshifted line-wing emission over $v_{\text{LSR}} = 25\text{--}30$ km s^{-1} , from 15 to 90 K km s^{-1} in steps of 15 K km s^{-1} .

[Snell et al. \(1984\)](#), the outflow contains $\sim 8 M_{\odot}$ of molecular gas. About half of this mass is at expansion velocities below 20 km s^{-1} . The other half belongs to the high-velocity outflow, which exhibits some of the brightest near-infrared (NIR) H₂ emissions in the sky. Peak 1, located $\sim 30''$ northwest of BN, is the strongest H₂-emitting region of the outflow (see Fig. 1).

The total H₂ line luminosity across the outflow is $120 \pm 60 L_{\odot}$ ([Rosenthal et al. 2000](#)). Observations of H₂ lines toward Peak 1 reveal excitation temperatures rising from ~ 600 K in the $v = 0$ rotational transitions, to ~ 2500 K in the vibrationally excited transitions ([Rosenthal et al. 2000](#); [Youngblood et al. 2018](#)). Observations suggest a more excited component at ~ 5000 K, likely caused by H₂ formation pumping after shock dissociation and reformation ([Geballe et al. 2017](#)). Peak 1 also exhibits excited CO and H₂O emission associated with warm, ~ 500 K, and hot, ~ 2500 K molecular gas ([González-Alfonso et al. 2002](#); [Goicoechea et al. 2015a](#)). In addition, low angular and spectral resolution FIR observations revealed bright [O I] fine-structure line emission (e.g., [Werner et al. 1984](#); [Herrmann et al. 1997](#); [Lerate et al. 2006](#); [Goicoechea et al. 2015a](#)) while *Herschel*/HIFI enabled the first velocity-resolved [C II] 158 μm maps of the region ([Goicoechea et al. 2015b](#); [Morris et al. 2016](#)).

The BN/KL outflow also shows intense OH emission, with $L_{\text{OH}}/L_{\text{H}_2\text{O}} \approx 0.4$, suggesting ongoing H₂O photodissociation ([Goicoechea et al. 2015a](#)). The low-lying OH rotational lines fall at FIR wavelengths, where the dust continuum is very intense. These lines require very high densities to be collisionally excited ($n_{\text{cr}} \gtrsim 10^{8-9} \text{ cm}^{-3}$) and are typically optically thick. As gas densities are typically lower, their excitation temperatures (T_{ex}) often fall below the continuum temperature, producing “P-Cygni” profiles in molecular outflows (first detected toward BN/KL; [Betz & Boreiko 1989](#); [Melnick et al. 1990](#); [Goicoechea et al. 2006a](#)).

3. SOFIA airborne observations and data reduction

We mapped multiple FIR lines with GREAT during 8 SOFIA flights between January 2014 and February 2021. Except for the flights in spring 2021 (observing cycle 8), which we operated out of Cologne-Bonn (CGN, Germany) during the pandemic, we carried out all flights from Palmdale, California. We conducted all observations during GREAT Consortium time (project IDs: 83_0004 (cycle 1), 83_0428 (cycle 4), and 83_0630 (cycles 8–9)). The flights accumulated 5 hours of total observing time.

In 2014, we performed the first observations of the OH ${}^2\Pi_{3/2}$ $J=5/2-3/2$ line (2514.3 GHz \approx 119.2 μm) with the single-pixel detector of GREAT (Heyminck et al. 2012). In 2021, we extended the map using the corresponding channel of the multi-color 4GREAT receiver (Duran et al. 2021). We observed the [O I] ${}^3P_1-{}^3P_2$ line (4744.8 GHz \approx 63 μm) with the 7-pixel high-frequency array (HFA) of upGREAT (Risacher et al. 2018). We simultaneously observed the [C II] ${}^2P_{3/2}-{}^2P_{1/2}$ line (1900.5 GHz \approx 158 μm) and the excited [O I] ${}^3P_0-{}^3P_1$ line (2060.1 GHz \approx 145 μm) with the two polarization-split upGREAT low-frequency sub-arrays (LFA): the 7-pixel V-polarization array tuned to the [O I] line and the H-polarization array to the [C II] line. This configuration processed 21 signals in parallel. During observations, we employed Fast Fourier Transform spectrometers, updated from Klein et al. (2012), which provided 32 k channels across the \sim 0.5–4 GHz intermediate-frequency bands. Table A.1 summarizes the instrument configurations.

The instrument and observatory performance (flight altitude, precipitable water vapor) determined the actual observing mode and source coverage (map sizes), and previous *Herschel* spectroscopic maps of Goicoechea et al. (2015a) guided them. Throughout this paper, we reference all observations to the nominal source position R.A. = $05^{\text{h}}35^{\text{m}}14.3^{\text{s}}$, Dec. = $-05^{\circ}22'33.7''$ (J2000) in the hot core region. We performed the upGREAT observations of both [O I] lines and [C II] in fast total power on-the-fly slewing mode (0.4 sec integration time per dump), using $3''$ sampling in both R.A. and Dec. We observed the source twice, scanning once in Dec. and once in R.A., with the fine sampling driven by the $6.3''$ beam of the HFA. The map size ($144'' \times 126''$) refers to the on-sky coverage of the central array pixels, while the hexagonal array's outer pixels provide a larger coverage. We selected a “clean” on-sky reference position at Δ R.A., Δ Dec. = $(-1700'', +900'')$. To achieve the most uniform sampling, we tilted the array axis by 19.1° relative to the scanning direction (Risacher et al. 2016a). We observed the OH ${}^2\Pi_{1/2}$ (1834.7 GHz \approx 163.4 μm) line during the LFA commissioning in 2016, using chopped (1 Hz) on-the-fly mode with $6''$ spatial sampling. The reference OH line frequencies (Table A.1) correspond to the line-strength-weighted frequency of each hyperfine-structure triplet, which are spectrally unresolved. We observed the OH 163.4 μm line of the Λ -doublet in the upper sideband, thereby avoiding to blend with the 163.1 μm line of the doublet in our dual sideband receiver.

We applied a large chop throw of $240''$ toward negative R.A. offsets. Observing the OH ${}^2\Pi_{3/2}$ 119.2 μm line proved most challenging. At this frequency, the shortage of local oscillator power needed to pump the HEB mixers forced us to couple the signal via a Martin–Puplett interferometer (Heyminck et al. 2012), which in turn limited the receiving bandwidth of the sky signal to \sim 1.6 GHz. Thus, the expected velocity coverage of the outflow barely fits into the effective bandpass (\sim 190 km s^{-1}). This asked for pointed (raster) observations, in double-beam chopped mode, for best system stability (wobbler throw $300''$, at -20° counter-clockwise against positive R.A.). In 2014, an exploratory 5×5 raster on a $10''$ grid was observed (with the single-pixel

M-channel of GREAT), showing the emission to be compact; in 2021 with 4GREAT we added a 5×5 raster on a $6''$ grid.

The GREAT consortium derived the half-power main beam sizes and efficiencies from planet observations. Telescope operators established the pointing on nearby optical reference stars with an accuracy of $1-2''$. At the beginning of each flight series, we aligned the optical axis of the instrument to these imagers by observing planets. Although the co-alignment between the central pixels is better than $1-2''$ (and the data header accounts for it), in this experiment we generally tracked the highest-frequency channel in a given configuration—typically the central HFA pixel in most flights. We amplitude-calibrated the raw data with the KOSMA *kalibrate* software (Guan et al. 2012). We corrected the data for atmospheric extinction and calibrated them in T_{mb}^2 . When SOFIA flew between 12.2–13.4 km in altitude, the atmospheric transmission remained smooth near the target velocities.

We processed the calibrated data with GILDAS³. We inspected the data to remove noisy spectra and other artifacts (e.g., spikes from onboard interference). We smoothed the spectra to a channel resolution of 0.15 km s^{-1} (0.3 km s^{-1} for the OH 119 μm line) and removed first-order baselines. The spectra were then gridded into a data cube through a convolution with a Gaussian kernel of full width at half maximum (FWHM) \sim 1/3 of the telescope beamwidth at the different frequencies. The 1σ rms noise levels in the maps are \sim 3.5 K ([O I] 63 μm), \sim 2.5 K ([O I] 145 μm), and \sim 2.0 K ([C II] 158 μm), and \sim 4.3 K (OH 163 μm) per velocity channel (as provided by the NOISE routine). To determine the noise over a given velocity bin, we used $\sigma_{\text{bin}} = \sigma_{\text{ch}} \delta v_{\text{ch}} \sqrt{N_{\text{ch}}}$, where σ_{ch} is the rms per channel, δv_{ch} the channel width, and N_{ch} the number of channels in that bin. Finally, for specific applications (e.g., line intensity ratio maps), we convolved the data cubes with Gaussian kernels to a common angular resolution, corresponding to FWHM values of $13''$ or $15''$.

4. Results

Figure 1 shows the core of OMC-1 observed with JWST/NIRCam F212N (McCaughrean & Pearson 2023), dominated by H₂ $v=1-0$ $S(1)$ line emission at 2.12 μm . The dashed square marks the field of view mapped with SOFIA/GREAT, encompassing the wide-angle BN/KL outflow, including the bright Peak 1 and Peak 2 regions. The cyan contours in Fig. 1 show the [O I] 63 μm redshifted line-wing emission at \sim 20 km s^{-1} relative to the cloud systemic velocity of \approx 8–9 km s^{-1} (hereafter $v_{\text{LSR},0}$; Bally et al. 1987; Berné et al. 2014). This [O I] emission peaks close to BN (Sect. 4.3) and follows the H₂ emission from the outflow. The field also includes the massive stars of the Trapezium cluster, in the foreground, located at \sim 0.2 pc in front of the cloud. Their far-UV (FUV; $6 < E < 13.6 \text{ eV}$) radiation, dominated by θ^1 Ori C star, illuminates all surfaces of OMC-1.

4.1. Integrated line intensity maps

Figure 2 shows [O I] 63, 145 μm , [C II] 158 μm , and OH 163 μm total line intensity maps (integrated over their complete line profile) in units of $\text{erg s}^{-1} \text{ cm}^{-2} \text{ sr}^{-1}$, which are used to compare the emitted line luminosity and line cooling budget. In these maps

² We shall refer to the “line luminosity” (L) in erg s^{-1} or L_{\odot} units. The conversion from integrated line intensity ($W = \int \Delta T_{\text{mb}} dv$) in K km s^{-1} , where ΔT_{mb} is the continuum-subtracted main brightness temperature, to integrated line intensity (I) in $\text{erg s}^{-1} \text{ cm}^{-2} \text{ sr}^{-1}$ is $I = 2k W \nu^3 / c^3$, or $I(\text{erg s}^{-1} \text{ cm}^{-2} \text{ sr}^{-1}) = W(\text{K km s}^{-1}) \cdot \nu(\text{GHz})^3 / 9.76 \cdot 10^{14}$.

³ see <http://www.iram.fr/IRAMFR/GILDAS>.

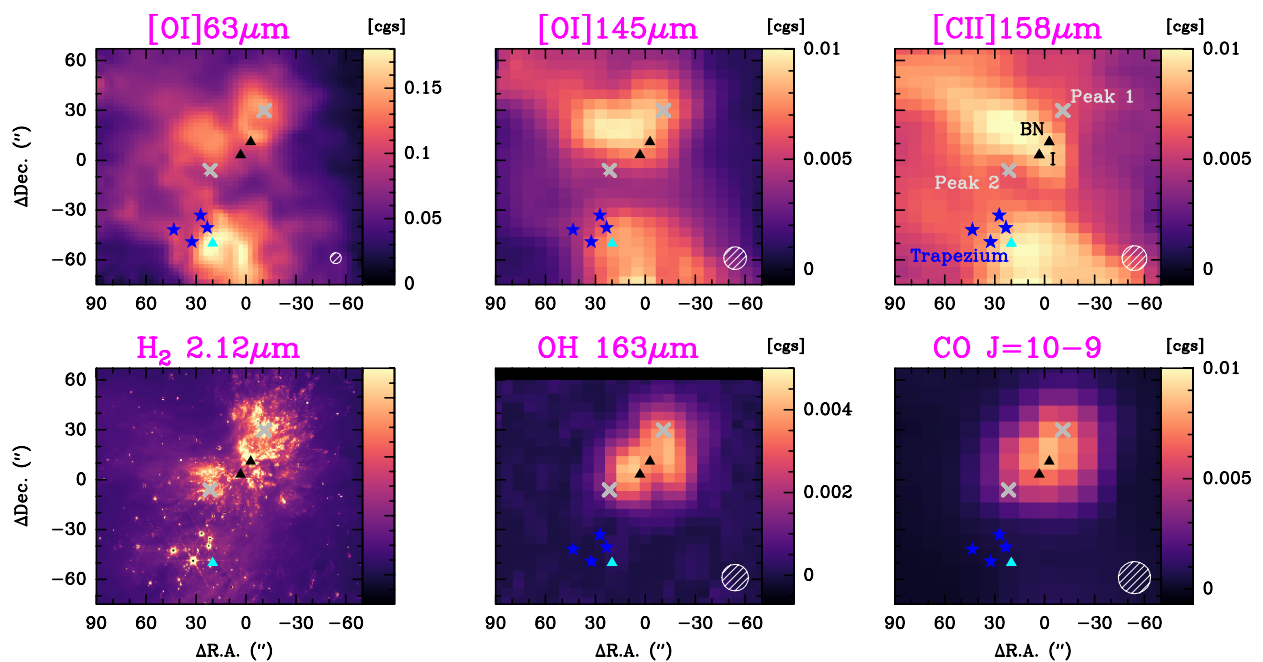


Fig. 2. Total line intensity maps (in $\text{erg s}^{-1} \text{cm}^{-2} \text{sr}^{-1} = \text{“cgs”}$) integrated over the complete line profile. The beam size is indicated in the bottom-right corner of each panel except for H_2 , where it is too small to display ($0.1''$). The cyan triangle shows a position near the Trapezium, where the $[\text{O I}] 63 \mu\text{m}$ line intensity peaks (Table D.1). The H_2 image refers to the JWST/NIRCam F212N image (McCaughrean & Pearson 2023). The $\text{CO } J = 10-9$ map was obtained with *Herschel*/HIFI at $20''$ resolution (Goicoechea et al. 2019).

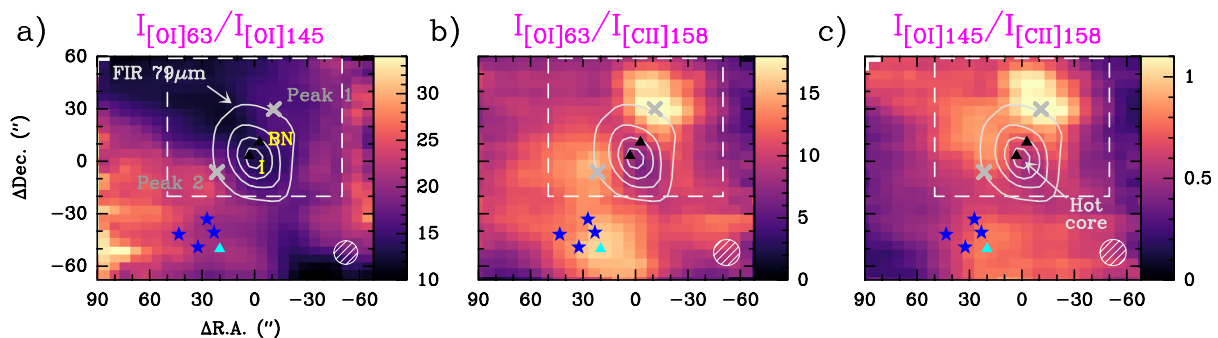


Fig. 3. Total line intensity ratio maps (derived from line intensities in $\text{erg s}^{-1} \text{cm}^{-2} \text{sr}^{-1}$). (a) $[\text{O I}] 63/145$ at a common angular resolution of $13''$, (b) $[\text{O I}] 63/[\text{C II}] 158$ at $15''$, and (c) $[\text{O I}] 145/[\text{C II}] 158$ at $15''$. The dashed box shows the $(100'' \times 80'')$ area used to extract both the line luminosities in the outflow region (Table 2) and the line intensities as a function of velocity (see Figs. 7 and 8). Contours show the FIR $79 \mu\text{m}$ -continuum emission obtained with *Herschel*/PACS, from 2.5 to 10 (10^3 Jy), centered at the position of the hot core (Goicoechea et al. 2015a).

we mark the positions of key stars (BN and source *I*) and environments (Peak 1, Peak 2, and the Trapezium region), which we study throughout the manuscript. The $[\text{O I}] 63 \mu\text{m}$ emission is the brightest FIR atomic fine-structure line in the region and roughly follows the H_2 emission along the wide-angle outflow. Still, the line intensity peaks southwest of the Trapezium stars, hereafter the “Trapezium position”, at $(+20'', -50'')$ from the map center (see details in Sect. 4.2). This region is part of the large-scale, face-on photodissociation region (PDR), with $n_{\text{H}} \gtrsim 10^5 \text{cm}^{-3}$ (e.g., Herrmann et al. 1997; Goicoechea et al. 2015b, 2019), at the interfaces between OMC-1 and the foreground H II region, which is photoionized by $\theta^1 \text{Ori C}$. This PDR component is located closer to the observer than the BN/KL outflow and produces bright narrow line emission—often called the “spike” component—at nearly all positions in the field.

The $[\text{O I}] 145 \mu\text{m}$ line is strikingly bright, as bright as the $[\text{C II}] 158 \mu\text{m}$ line, and shows a similar spatial distribution as the $[\text{O I}] 63 \mu\text{m}$ emission. As observed before (e.g., Goicoechea et al. 2015b; Morris et al. 2016), the

$[\text{C II}] 158 \mu\text{m}$ integrated intensity map does not follow the H_2 emission. Instead, $[\text{C II}] 158 \mu\text{m}$ shows strong emission close to the Trapezium, along with lower line intensity emission from the FUV-irradiated surface of OMC-1. The $\text{OH } ^2\Pi_{1/2} J=3/2-1/2$ line emission at $163 \mu\text{m}$ is confined to the outflow, peaking toward the inner hot core region, with only very faint emission from the quiescent cloud and PDR. The spatial distribution of the $\text{OH } 163 \mu\text{m}$ emission resembles that of the high- J CO emission (e.g., Peng et al. 2012; Goicoechea et al. 2015a, 2019).

Figure 3 shows the atomic fine-structure line intensity ratio maps (integrated over the entire line profile). Typically, these intensity ratios provide diagnostics of the gas density, temperature, and FUV radiation field strength in the warm gas associated with PDRs and shocks. Although these maps do not reveal the velocity structure of the gas, they display a different spatial distribution compared to the absolute line intensity maps (Fig. 2). The $[\text{O I}] 63/[\text{C II}] 158$ intensity ratio map shows a clear maximum (≈ 20) toward Peak 1 (Fig. 3b). The $[\text{O I}] 145/[\text{C II}] 158$ map exhibits a similar spatial distribution, with a high ratio ($\gtrsim 1$)

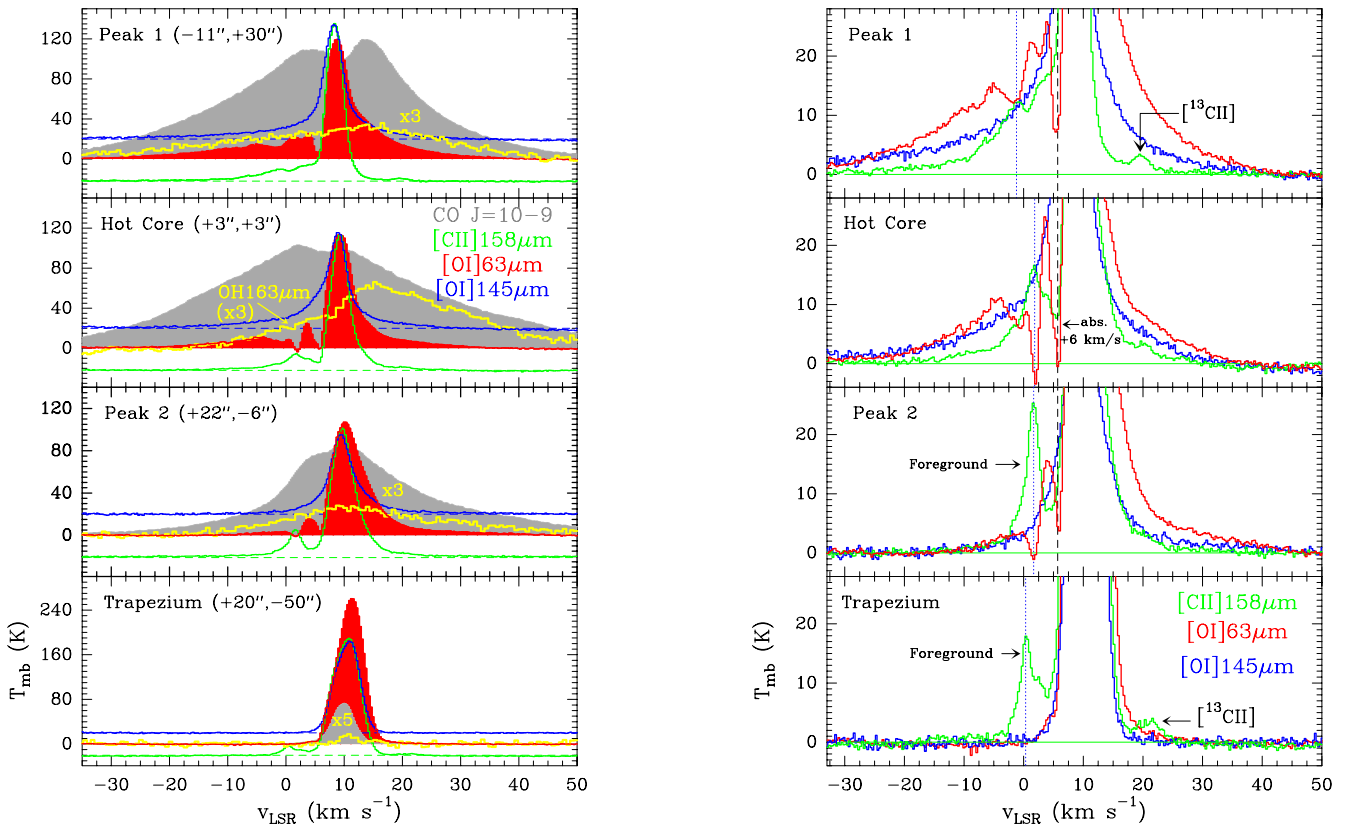


Fig. 4. Velocity-resolved spectra at representative positions, all from maps convolved to $15''$ (except CO 10–9, with a beam of $20''$). *Left:* Complete spectra, with offsets in arcseconds given in parenthesis; continuum levels of [C II] $158\ \mu\text{m}$ and [O I] $145\ \mu\text{m}$ shifted for clarity. The OH $163\ \mu\text{m}$ emission lines (yellow) are scaled by a factor of three or five. *Right:* Zoom on faint line wings and foreground line features.

toward Peak 1 (Fig. 3c). Given the much higher critical densities for collisional excitation (n_{cr}) of the [O I] 63 and $145\ \mu\text{m}$ lines compared to that of the [C II] $158\ \mu\text{m}$ line (see Table A.1), these peaks trace the highest-density gas (assuming similar FUV illumination). In general, the [O I] 63/[C II] $158\ \mu\text{m}$ line intensity ratios toward Peak 1 are higher than those observed toward protostellar outflows (e.g., Liseau et al. 2006) and PDRs (e.g., Bernard-Salas et al. 2012). Figure 3 (contours) also shows the FIR continuum map at $79\ \mu\text{m}$ (Goicoechea et al. 2015b), tracing the extended warm dust emission from the hot core region. The continuum emission is fainter toward the Peak 1 and Peak 2. The [O I] 63/ $145\ \mu\text{m}$ ratio shows its lowest values (≈ 10) in a region roughly orthogonal to the wide-angle outflow (Fig. 3a), following the quiescent cloud, the “extended ridge”. Radiative transfer models (Sect. 5.2) indicate that the low intensity ratios are consistent with the [O I] $63\ \mu\text{m}$ line being optically thick, and with the gas having lower density than in the postshock gas.

4.2. Velocity-resolved far-infrared line profiles

4.2.1. Line wings

The GREAT maps allow us to resolve the velocity structure of the [O I] 63 and $145\ \mu\text{m}$ emission and to compare it with other FIR lines: [C II] $158\ \mu\text{m}$, OH, and high- J CO. Figure 4 presents such a comparison for four representative positions: Peak 1, the hot core region, Peak 2, and the Trapezium position. The first three positions lie on the outflow region and show line wing emission. As is apparent from these spectra, the OH and CO lines exhibit similarly broad line profiles, with $\Delta v_{\text{FWHM}} \gtrsim 30\ \text{km s}^{-1}$. These lines exhibit prominent wings, with full widths at zero intensity

(FWZI) exceeding $150\ \text{km s}^{-1}$ (see Fig. 5 and Kwan & Scoville 1976; Zapata et al. 2009; Peng et al. 2012, for additional velocity-resolved CO studies). These line profiles differ markedly from those of the FIR atomic fine-structure lines (Fig. 4), which consist of a bright narrow component, $\Delta v_{\text{FWHM}} \approx 4\ \text{km s}^{-1}$, together with moderately broad wings. This suggests that the shocks producing the atomic fine-structure emission differ in nature or location from those driving the highest-velocity CO and OH emission.

The FWZI of the [O I] 63 and $145\ \mu\text{m}$ lines toward Peak 1 is $\sim 85\ \text{km s}^{-1}$ and $\sim 62\ \text{km s}^{-1}$, respectively. The [O I] FWZIs exceed that of the [C II] $158\ \mu\text{m}$ line ($\lesssim 50\ \text{km s}^{-1}$). This implies that the highest-velocity component either lacks FUV illumination or that C^+ is rapidly converted into other species in the postshock gas (see also Morris et al. 2016). The [O I] $145\ \mu\text{m}$ line is optically thin and is not affected by foreground absorptions (see Sect. 4.2.3). Toward Peak 1, the line profile can be fitted with two Gaussians of similar intensity but different line FWHM: a narrow one ($\Delta v_{\text{FWHM}} \approx 3.6 \pm 0.1\ \text{km s}^{-1}$ centered at $v_{\text{LSR}} \approx +8.2 \pm 0.1\ \text{km s}^{-1}$), consistent with gas in the quiescent face-on PDR, and a broad one ($\Delta v_{\text{FWHM}} \approx 19.6 \pm 0.3\ \text{km s}^{-1}$ at $v_{\text{LSR}} \approx +7.4 \pm 0.1\ \text{km s}^{-1}$), implying supersonic velocity dispersions associated with shocked gas.

In Appendix B, we show the velocity channel maps of the observed FIR lines. As in Fig. 1, the redshifted [O I] 63 and $145\ \mu\text{m}$ emission follows the H_2 and CO emission along the two lobes of the wide-angle outflow, whereas the redshifted [C II] $158\ \mu\text{m}$ emission is weak toward Peak 1 and Peak 2 (Fig. B.1). The [O I] 63 and $145\ \mu\text{m}$ emission from the blueshifted wing peaks around BN and Peak 1. At $v_{\text{LSR},0}$, the atomic lines show extended emission in the SW–NE direction, orthogonal to the wide-angle outflow, mostly tracing the illuminated rim of OMC-1’s ridge.

Assuming that most of the narrow-line emission arises from the face-on PDR at the rims of OMC-1, as suggested by its spatial distribution (see also Fig. B.1), we estimate that $\sim 65\%$, $\sim 50\%$, and $\sim 15\%$ of the observed [O I] 63, [O I] 145, and [C II] 158 μm emissions, respectively, originate from shocked gas. Nonetheless, some of the narrow line emission may originate from low-velocity outflows or from shocks oblique to the line of sight, so the above percentages should be considered lower limits.

4.2.2. [O I] 63 μm narrow-line “spike” emission

For bright, optically thick [O I] 63 μm emission, the continuum-subtracted peak main-beam temperature, $T_P = J(T_{\text{ex}}) - J(T_{\text{dust}})$, where $J(T)$ is the Planck-corrected radiation temperature, yields the excitation temperature, T_{ex} , of the line, arising here from the extended PDR in front of the outflow:

$$T_{\text{ex}}([\text{O I}] 63 \mu\text{m}) = \frac{227.7}{\ln\left(1 + \frac{227.7}{T_P([\text{O I}] 63 \mu\text{m}) + J(T_{\text{dust}})}\right)} \text{ K}, \quad (1)$$

where $\Delta E/k_B = (E_u - E_l)/k_B = 227.7 \text{ K}$ is the equivalent temperature of the transition, and $J(T_{\text{dust}}) = T_c$ is the continuum brightness temperature at 63 μm . In most observed positions, $T_P([\text{O I}] 63 \mu\text{m}) \approx 100\text{--}120 \text{ K}$, and $J(T_{\text{dust}}) \approx 5\text{--}100 \text{ K}$ (from the 63 μm continuum levels of Werner et al. 1984), where the highest value refers to the hot core region. These $T_P([\text{O I}] 63 \mu\text{m})$ values translate to $T_{\text{ex}} \gtrsim 200 \text{ K}$, which is a lower limit to the gas temperature (e.g., Fig. C.2).

Far from the outflow, the atomic fine-structure lines are narrow and lack high-velocity wings. This is exemplified by the spectra toward the Trapezium position (Fig. 4), where these lines show Gaussian profiles and line FWHM of about 5 km s^{-1} (Table D.1). Still, this particular position—resembling a cavity structure—shows remarkably strong [O I] 63 μm emission, with a peak brightness temperature of $T_{\text{peak}} = 330 \text{ K}$ (at the native $6''$ resolution). This implies $T_k \geq T_{\text{ex}} \approx 440 \text{ K}$ (with $T_c \approx 5 \text{ K}$, and assuming a beam filling of one), consistent with warm-to-hot gas in a dense PDR facing the Trapezium. This excited PDR is located near the region of maximum CH⁺ $J = 1\text{--}0$ emission in OMC-1 (position #3 of Goicoechea et al. 2019), a signature of strong FUV irradiation and elevated temperatures. JWST images reveal this and similar cavities illuminated by FUV radiation from the Trapezium; e.g., Fig. 4 of McCaughrean & Pearson (2023) and Fig. 4 of Habart et al. (2024). These “crenellations” (O’Dell et al. 2015) at OMC-1’s illuminated surface were likely carved by protostellar outflows (see also Kavak et al. 2022).

4.2.3. Foreground [O I] 63 μm line absorption

The [O I] 63 μm line is a ground-state transition. The strong dust continuum at 63 μm from the central BN/KL region (Werner et al. 1976; Cernicharo et al. 2006; Goicoechea et al. 2015b), together with the presence of low excitation gas along the line of sight, produces absorption features in the blueshifted [O I] 63 μm line wing, where $T_{\text{ex}} < T_c$. In this region, the [O I] 63 μm line profile shows a narrow, a few km s^{-1} FWHM, absorption component at $v_{\text{LSR}} \approx +6 \text{ km s}^{-1}$, which is typically associated with gas in the hot core itself (e.g., Blake et al. 1987; Tercero et al. 2010). In addition, it shows blue-shifted absorptions, at $v_{\text{LSR}} \approx -1 \text{ km s}^{-1}$ (toward Peak 1) and at $v_{\text{LSR}} \approx +2 \text{ km s}^{-1}$ (toward the hot core and Peak 2). These blueshifted absorptions coincide with [C II] 158 μm emission peaks (left panels of Fig. 4) known to arise from foreground material in Orion’s Veil (Goicoechea et al. 2015b; Pabst et al. 2019), including the

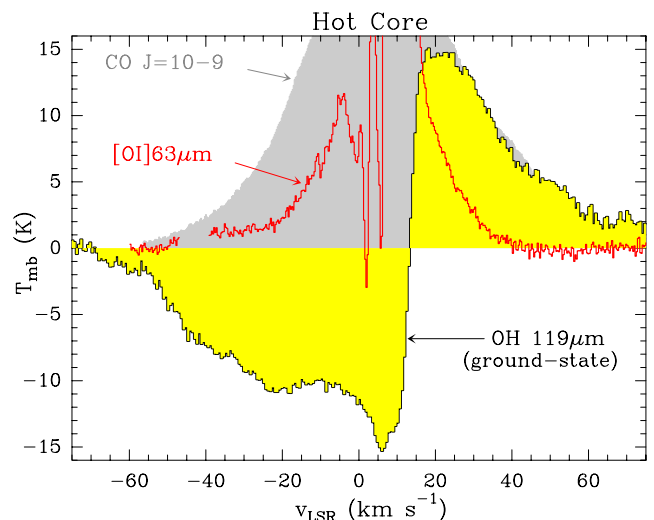


Fig. 5. P-Cygni profile of the OH 119 μm line toward the hot core region (the FIR continuum peak), compared to other line profiles. See Fig. B.3 for a zoom on the low-intensity features.

“Northern Dark Lane” and the “Dark Bay”, which are apparent in optical images (O’Dell 2001). Because of the lower density in these components ($n_{\text{H}} \approx 10^3 \text{ cm}^{-3}$; Pabst et al. 2020), the fainter 158 μm continuum, and the much lower critical density of the [C II] 158 μm transition, leading to $T_{\text{ex}} > T_c$, these foreground gas layers appear as [C II] 158 μm emission components. Away from the hot core region, the [O I] 63 μm line profiles show no absorption components.

4.2.4. OH P-Cygni profiles from the high-velocity outflow

Figure 4 (left panel, yellow histograms) display the OH ${}^2\Pi_{1/2} J=3/2\text{--}1/2$ line profile (one of the Λ -doublets of the excited OH 163 μm transition). These observations have much higher angular and spectral resolution than previous observations with the Kuiper Airborne Observatory (KAO), the Infrared Space Telescope (ISO), and Herschel (Melnick et al. 1987, 1990; Goicoechea et al. 2006a, 2015a). The OH 163 μm line profile toward Peak 1 shows a very broad profile, with a FWZI of $\gtrsim 150 \text{ km s}^{-1}$ and $\Delta v_{\text{FWHM}} \approx 40 \text{ km s}^{-1}$, thus comparable to the CO lines (e.g., Kwan & Scoville 1976; Snell et al. 1984; Zapata et al. 2009; Peng et al. 2012; Bally et al. 2017). As opposed to the atomic fine-structure lines, the OH 163 μm emission does not show a narrow line component. Indeed, the line is very faint toward the Trapezium position (Figure 4), implying that the broad-line emission originates in shocked gas and regions subject to strong radiative pumping, but not from the quiescent cloud gas. This rotationally excited OH line arises from the first excited state (at $E_u/k = 270 \text{ K}$) of the ${}^2\Pi_{1/2}$ ladder. Given its high excitation requirements ($n_{\text{cr}} \approx 10^9 \text{ cm}^{-3}$), the upper level can only be populated either by collisions in very dense, warm gas, and/or by absorption of FIR dust photons in the ${}^2\Pi_{1/2}\text{--}{}^2\Pi_{3/2}$ cross-ladder transition at $\sim 53 \mu\text{m}$ (e.g., Goicoechea & Cernicharo 2002; Goicoechea et al. 2006a). Owing to the different dust continuum levels, the latter process contributes to the hot core region, while the former likely dominates in Peak 1 and Peak 2, with possible lateral (i.e., not along the line of sight) FIR illumination from the hot core. The broad OH 163 μm line profiles trace the outflow at all velocities, and the line intensity tends to peak toward the hot core (see also Fig. B.1), where the effect of FIR pumping is strongest.

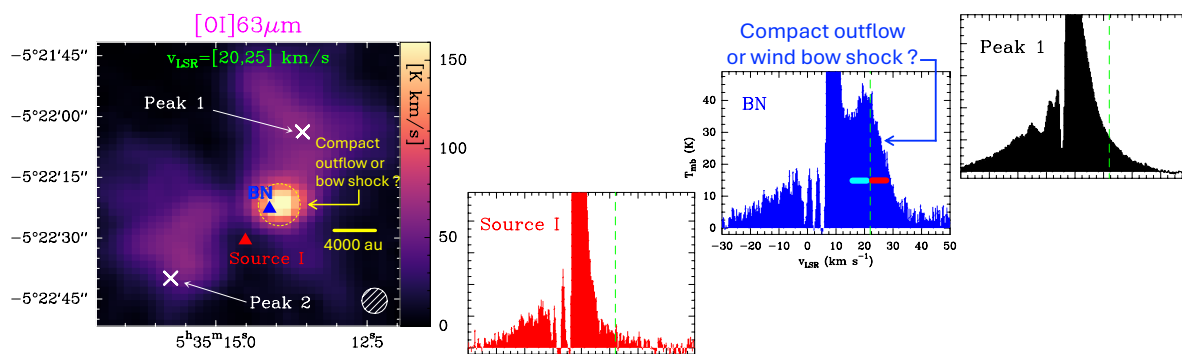


Fig. 6. Possible compact outflow or wind bow shock around BN star. *Left:* Spatial distribution of the redshifted [O I] 63 μm emission in the v_{LSR} range from +20 to +25 km s^{-1} . This map (in R.A. and Dec.) shows extended emission following the wide-angle H_2 outflow and a possible spatially unresolved outflow around BN, revealed as a distinct broad spectral component. *Right:* [O I] 63 μm spectra toward Source I (red), BN (blue), and Peak 1 (black). Only the blue spectrum shows the broad spectral feature around the LSR velocity of BN (dashed green line).

Figure 5 compares the [O I] 63 μm , CO $J=10-9$, and OH $^2\Pi_{3/2} J=5/2-3/2$ (one of the Λ -doublets of the OH 119 μm ground-state transition) line profiles toward the hot core position, roughly the FIR dust continuum peak. The [O I] 63 μm spectrum shows the three absorption components at $v_{\text{LSR}} \approx +6$, $+2$, and -1 km s^{-1} . The first component is consistent with gas in the hot core, while the other two originate from foreground gas associated with Orion’s Veil. Betz & Boreiko (1989) provided the first sub- km s^{-1} resolution observations of the OH 119 μm rotational line with the KAO. These observations revealed a self-absorption profile, characterized by absorption on the blueshifted side and emission on the redshifted side. The SOFIA telescope delivers a factor of three better angular resolution ($11.3''$ at 119 μm), which provides less angular dilution of the FIR continuum source. The resulting OH 119 μm line shows a more prominent P-Cygni profile (the line shows absorption and emission of similar strength), with a FWZI of ≈ 160 km s^{-1} , much like CO lines. Compared to Betz & Boreiko (1989), SOFIA observations show that the entire blueshifted wing is absorbed from $v_{\text{LSR}} \approx -80$ to $+8.5$ km s^{-1} , while the redshifted emission extends up to $v_{\text{LSR}} \approx +80$ km s^{-1} , with a velocity coverage similar to that of the CO $J=10-9$ line. Clearly, OH is present in the high-velocity outflowing gas, with terminal (maximum) velocities of about 80 km s^{-1} –the fastest gas producing absorption projected along the line of sight. A closer examination of the OH 119 μm P-Cygni profile reveals that the main absorption dip occurs at $v_{\text{LSR}} \approx +6$ km s^{-1} , which corresponds to the hot core absorption (for a zoomed-in spectrum, see Fig. B.3). We leave a detailed analysis of the OH excitation to a forthcoming paper.

4.3. A possible outflow or wind bow shock around BN

Figure 6 (left) shows a map of the [O I] 63 μm emission in the v_{LSR} range from +20 to +25 km s^{-1} . In addition to the redshifted extended emission from the explosive outflow, we detect an emission peak near BN, located slightly northwest (NW) of this young massive star ($\sim 8-13 M_{\odot}$; e.g., Rodríguez et al. 2005). This emission does not coincide with the more extended, so-called low-velocity “18 km s^{-1} outflow”, which expands in the SW–NE direction (Genzel et al. 1981; Plambeck et al. 1982) and is likely driven by Source I (Beuther & Nissen 2008; Wright et al. 2022). The new [O I] 63 μm component arises from a broad emission feature, with a line FWHM of 15 ± 1 km s^{-1} , centered at $v_{\text{LSR}} \approx 20$ km s^{-1} (blue spectrum in Fig. 6). This emission is confined to the vicinity of BN, indicating either a compact outflow or a knot or shell of shock-excited gas surround-

ing the star. It envelops the IR nebulosity associated with BN (see Shuping et al. 2004; Bally et al. 2020) but has not been reported in other line tracers, likely owing to the nature of this shocked gas and the complex substructure of the region in terms of emission, velocity, and extinction.

The centroid of the [O I] 63 μm line feature is compatible with the LSR velocity measured from emission lines associated with BN ($v_{\text{LSR}} \approx 23$ km s^{-1} ; Gómez et al. 2008; Goddi et al. 2011; Plambeck et al. 2013). The apparent extent of this [O I] 63 μm spectral feature is $< 10''$ and remains undetected at 145 μm . The blue- and red-shifted [O I] 63 μm emission around the LSR velocity of BN shows a similar spatial distribution, suggesting that, if it originates from an outflow, the outflow is spatially unresolved. Given the uncertain properties of BN’s circumstellar disk, particularly its geometry (Jiang et al. 2005; Beuther et al. 2010; Bally et al. 2020), it remains unclear whether this structure traces a disk-driven outflow or another form of shocked gas.

Interestingly, the [O I] 63 μm intensity peak is shifted to the NW of BN by $\lesssim 3''$, and is roughly aligned with the proper motion of this runaway star. Thus, this [O I] 63 μm emission may correspond to an unresolved wind bow shock produced by the interaction of BN’s supersonic motion and wind with the ambient cloud gas (Baranov et al. 1971; Wilkin 1996). Adopting estimates of the wind mass-loss rate (\dot{M}_w), wind velocity (v_w), and BN’s velocity (v_*) relative to the surrounding cloud of density n_0 (Scoville et al. 1983; Bally et al. 2020), the bow-shock radius (r_{bs}) would be several hundred au, or $\lesssim 1''$ (Tan 2004). However, the wind mass-loss rate and velocity remain uncertain. Since $r_{\text{bs}} \propto (\dot{M}_w v_w / n_0)^{1/2} v_*^{-1}$, larger wind parameters would yield a correspondingly larger r_{bs} (for fixed n_0 and v_*), potentially consistent with the apparent size of the [O I] 63 μm feature.

5. Analysis

In the following, we restrict our analysis to a $100'' \times 80''$ ($0.2 \text{ pc} \times 0.16 \text{ pc}$) region around the explosive outflow, indicated with a dashed square in Fig. 3. That is, we exclude the Trapezium region. In addition, we use the spectra toward Peak 1 as a template to determine the physical conditions of the postshock gas.

5.1. Velocity-resolved line intensity ratios

Figure 7 shows the FIR line intensity ratios as a function of velocity toward Peak 1 position (filled squares) obtained from maps convolved to a common angular resolution of $15''$. The lowest

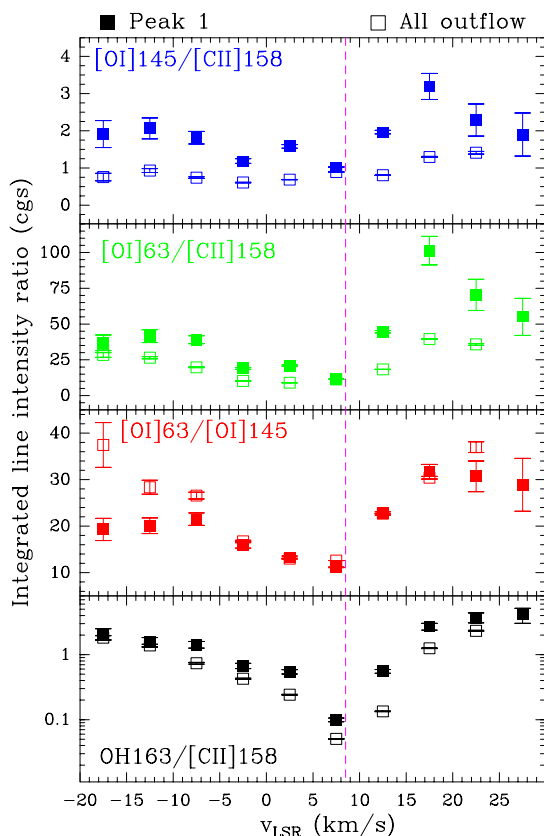


Fig. 7. FIR line intensity ratios as a function of velocity in a $15''$ beam toward Peak 1 (filled squares) and averaged over the $100'' \times 80''$ region of the BN/KL outflow (empty squares), binned in intervals of 5 km s^{-1} from maps convolved to a common angular resolution of $15''$. The dashed magenta line marks the LSR velocity of the quiescent gas in OMC-1.

$[\text{O I}] 63/145$ line intensity ratio, 11.4 ± 0.1 , occurs at $v_{\text{LSR},0}$, corresponding to the LSR velocity of the quiescent gas in OMC-1 (dashed magenta line in Fig. 7), where the narrow line component is dominated by emission from the extended PDR in front of the outflow. This intensity ratio is comparable to that observed in the Orion Bar (e.g., Bernard-Salas et al. 2012). The $[\text{O I}] 63/145$ intensity ratio then increases in the line wings, reaching ~ 30 at redshifted velocities. The $[\text{O I}] 63/145$ intensity ratio shows an asymmetry between the blue- and red-shifted wings. Foreground $[\text{O I}] 63 \mu\text{m}$ absorption at v_{LSR} between roughly -5 and $+7 \text{ km s}^{-1}$ contributes to this asymmetry, but the blueshifted wing shows smaller ratios at higher, more negative velocities (see also Fig. B.2). These lower ratios suggest a correspondingly lower density in the blueshifted postshock gas (Sect. 5.2).

Figure 7 also shows the velocity dependence of the $[\text{O I}] 145/[\text{C II}] 158$, $[\text{O I}] 63/[\text{C II}] 158$, and $\text{OH } 163/[\text{C II}] 158$ line intensity ratios. All these ratios reach a minimum at the LSR velocity of the face-on PDR, $v_{\text{LSR},0}$, and gradually increase in the line wings, indicating a lower contribution of C^+ in the highest-velocity gas. The $[\text{O I}] 145 \mu\text{m}$ line is particularly bright, with $[\text{O I}] 145/[\text{C II}] 158$ intensity ratios of $\approx 2\text{--}3$ in the line wings. The $\text{OH } 163/[\text{C II}] 158$ line intensity ratio increases from ≈ 0.1 at the line center to 4 ± 1 in the wings, thus showing a strong dependence on radial velocity. The redshifted line wing shows very high $[\text{O I}] 63/[\text{C II}] 158$ intensity ratios, up to $\approx 50\text{--}100$, much higher than the expected ratios in PDRs with $n_{\text{H}} \approx 10^5 \text{ cm}^{-3}$ (e.g., Kaufman et al. 1999). For reference, in the prototypical dense PDR, the Orion Bar, at $\sim 2'$ south of the Trapezium, these line intensity ratios

are much lower, $[\text{O I}] 63/145 \approx 9$, $[\text{O I}] 63/[\text{C II}] 158 \approx 8$, $[\text{O I}] 145/[\text{C II}] 158 \approx 0.9$, and $\text{OH } 163/[\text{C II}] 158 \approx 0.03$ (e.g., Bernard-Salas et al. 2012; Joblin et al. 2018).

The empty squares in Fig. 7 show the FIR line intensity ratios as a function of LSR velocity, averaged over the $100'' \times 80''$ region, thus representing the average conditions in the outflow. These ratios are roughly similar to those toward Peak 1, with the main differences being a slightly higher $[\text{O I}] 63/145$ intensity ratio in the blueshifted wing and slightly lower $[\text{O I}] 145/[\text{C II}] 158$, $[\text{O I}] 63/[\text{C II}] 158$, and $\text{OH } 163/[\text{C II}] 158$ intensity ratios. This reflects the higher relative contribution of the $[\text{C II}] 158 \mu\text{m}$ line⁴ in the SE part of the outflow (see Figs. 3b and 3c). Figure B.2 shows these results in the form of intensity-ratio velocity channel maps. These maps illustrate the same trends described above: the $[\text{O I}] 63/[\text{C II}] 158$ and $[\text{O I}] 145/[\text{C II}] 158$ intensity ratios in the redshifted wing peak toward Peaks 1 and 2, following the H_2 outflow. These regions coincide with enhanced $[\text{O I}] 63/145$ intensity ratios.

Table 1 summarizes the intensities of the atomic fine-structure lines toward Peak 1, measured in three velocity intervals of the line profile: the redshifted wing, the blueshifted wing, and the narrow component. To increase the S/N of the line-intensity measurements and to cover the relevant outflow velocity range, we derived the wing intensities using velocity bins of 25 km s^{-1} in the wings. We adopted the $[-30, -5]$ and $[+21, +46]$ km s^{-1} LSR velocity intervals for the redshifted and blueshifted wings, respectively. That is, radial velocities of 13 to 38 km s^{-1} with respect to $v_{\text{LSR},0}$. This choice excludes the velocity ranges of the $[\text{O I}] 63$ and $[\text{C II}] 158 \mu\text{m}$ lines that are affected by foreground absorption and emission in the blueshifted wing (see Fig. 4). We also subtracted the contribution of the $[\text{C II}] F=2-1$ hyperfine-structure line in the redshifted wing using multi-Gaussian fitting. In Sect. 6.2, we use these line-wing intensities to constrain the nature of the shocks that give rise to the FIR atomic line emission.

5.2. Postshock gas physical conditions and $[\text{O I}] 63, 145 \mu\text{m}$ excitation across different outflow velocity components

The observed $[\text{O I}] 63/[\text{O I}] 145 \mu\text{m}$ intensity ratios (I_{63}/I_{145}) in the line wings are high, reaching up to ~ 30 (e.g., Table 1). This is close to the high-temperature limit for optically thin emission under local thermodynamic equilibrium (LTE⁵) conditions ($T_{\text{ex}} = T_{\text{k}}$). This would imply $N(\text{O}) < \text{a few } 10^{18} \text{ cm}^{-2}$ and high densities, meaning $n_{\text{H}} \gg n_{\text{cr}}$, with $n_{\text{cr}, 63 \mu\text{m}} \approx 5 \times 10^5 \text{ cm}^{-3}$ and $n_{\text{cr}, 145 \mu\text{m}} \approx 6 \times 10^6 \text{ cm}^{-3}$ for optically thin emission. However, LTE is rarely fulfilled, and even for a three-level system such as the $^3\text{P}_J$ levels of atomic oxygen, subtle non-LTE, line opacity, and FIR pumping effects can dominate the $[\text{O I}]$ line emission, thus, the resulting I_{63}/I_{145} ratio (Monteiro & Flower 1987; Elitzur & Asensio Ramos 2006; Goicoechea et al. 2009; Goldsmith 2019).

To estimate the beam-averaged physical conditions (n_{H} , T_{k}) and the atomic oxygen column densities, $N(\text{O})$, in the postshock gas across the different velocity components, we used a nonlocal, non-LTE radiative transfer model (Goicoechea et al. 2006b, 2009) with up-to-date O-H_2 and O-H inelastic collision rate coefficients (Lique et al. 2018). This nonlocal approach accounts for $[\text{O I}] 63 \mu\text{m}$ line opacity and line trapping, as well as $[\text{O I}] 145 \mu\text{m}$ suprathermal excitation ($T_{\text{ex}} > T_{\text{k}}$) and population inversions, which local single escape probability methods fail

⁴ The $[\text{C II}] 158 \mu\text{m}$ emission around $v_{\text{LSR}} \approx +20 \text{ km s}^{-1}$ can be dominated by $[\text{C II}] F=2-1$ emission from OMC-1 (right panels of Fig. 4).

⁵ In the optically thin LTE regime, $I_{63}/I_{145} = 35.3 e^{+98.8/T_{\text{k}}}$, where $[E(^3\text{P}_0) - E(^3\text{P}_1)]/k = 98.8 \text{ K}$ (see also Goldsmith 2019).

Table 1. FIR atomic fine-structure line intensities and intensity ratios at different velocities toward Peak 1 and the Orion Bar PDR (for reference).

$[v_{\text{LSR}} \text{ range}]$	[O I] 63 μm	[O I] 145 μm	[C II] 158 μm			
Source (km s $^{-1}$)	($\times 10^{-2}$ erg s $^{-1}$ cm $^{-2}$ sr $^{-1}$)	($\times 10^{-4}$ erg s $^{-1}$ cm $^{-2}$ sr $^{-1}$)	I_{63}/I_{145}	I_{63}/I_{158}	I_{145}/I_{158}	
Red wing: [+21, +46]	1.0 \pm 0.1	3.7 \pm 0.4	1.7 \pm 0.3	27 \pm 4	59 \pm 10	2.2 \pm 0.4
Blue wing: [-30, -5]	1.8 \pm 0.1	9.8 \pm 0.4	4.9 \pm 0.3	18 \pm 1	37 \pm 3	2.0 \pm 0.1
Narrow: [+5, +10]	4.0 \pm 0.1	36.0 \pm 0.2	35.0 \pm 0.1	11 \pm 1	11 \pm 1	1.0 \pm 0.1
Orion Bar PDR \ddagger	19 \pm 5	210 \pm 40	230 \pm 90	9 \pm 3	8 \pm 4	0.9 \pm 0.4

Notes. In a beam of 15'' from maps convolved to a common resolution of 15''. \ddagger From *Herschel*/PACS (Bernard-Salas et al. 2012; Joblin et al. 2018).

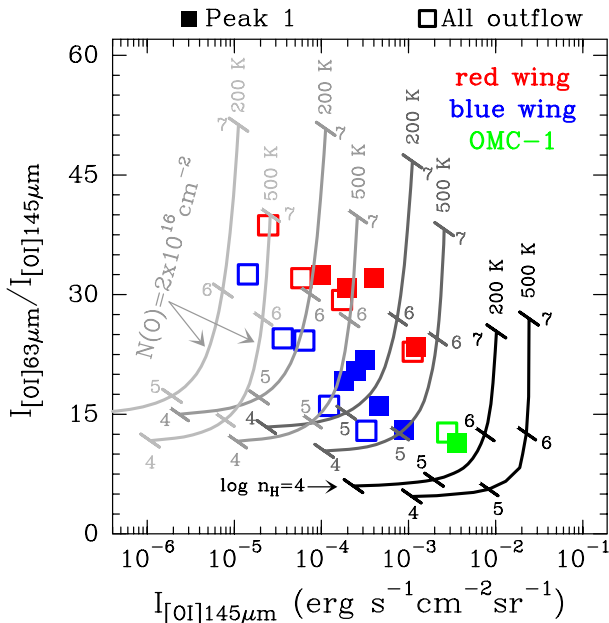


Fig. 8. [O I] 63/145 μm line intensity ratio versus [O I] 145 μm line intensity. The light grey to black curves show a grid of radiative transfer models for four values of $N(\text{O})$: 2×10^{16} , 2×10^{17} , 2×10^{18} , and 2×10^{19} cm $^{-2}$, from left to right, at 200 and 500 K. Tick marks denote $\log n_{\text{H}}$ (in cm $^{-3}$) and are separated by one decade along curves of constant $N(\text{O})$. The colored squares show the observed values in LSR velocity bins of 5 km s $^{-1}$ toward Peak 1 (filled squares) and averaged over the BN/KL outflow (open squares). Red squares correspond to the redshifted line wing, while blue squares correspond to the blueshifted line wing. Green squares correspond to OMC-1 velocities (see text and Tables D.2 and D.3).

to correctly capture. To match the observed [O I] 145 μm line FWHM (broad component), we adopted a turbulent line width of 20 km s $^{-1}$. Following Goicoechea et al. (2009), we also examined the impact of FIR radiative pumping on the [O I] fine-structure level populations. Appendix C provides details and explores the excitation conditions over a wide parameter space.

Figure 8 presents the results of a model grid displayed in the velocity-dependent parameter space $I_{63}/I_{145}(v)$ versus $I_{145}(v)$. The light grey to black curves show radiative transfer models for four atomic oxygen column densities, from 2×10^{16} to 2×10^{19} cm $^{-2}$, increasing from left to right, at two gas temperatures, 200 and 500 K. Tick marks denote $\log n_{\text{H}}$ (in cm $^{-3}$) and are separated by one decade along curves of constant $N(\text{O})$. In general, as the opacity of the [O I] 63 μm line increases, the intensity ratio I_{63}/I_{145} decreases roughly as $\sim 1/\tau_{63}$, while the [O I] 145 μm line is rarely optically thick. In dense gas, intensity ratios $I_{63}/I_{145} \lesssim 15$ typically imply optically thick [O I] 63 μm emission. For the adopted parameters, the gas density also de-

termines the [O I] excitation regime. For $n_{\text{H}} \gtrsim n_{\text{crit}}$, the I_{63}/I_{145} ratio increases with n_{H} owing to a significant increase in the [O I] 63 μm excitation temperature and a decrease in τ_{63} toward the optically thin regime. In this regime, the ratio also increases with decreasing gas temperature. The colored squares in Fig. 8 represent the observed values in LSR velocity bins of 5 km s $^{-1}$ toward Peak 1 (filled squares) and averaged over the BN/KL outflow (open squares). Red squares correspond to the redshifted line wing, in the range [+10, +25] km s $^{-1}$, while blue squares correspond to the blueshifted line wing, [-20, 0] km s $^{-1}$. Green squares in Fig. 8 correspond to the quiescent cloud gas at OMC-1 velocities, $v_{\text{LSR}} = [+5, +10]$ km s $^{-1}$. The green squares are consistent with large column densities of atomic oxygen, $N(\text{O}) \approx 10^{19}$ cm $^{-2}$, optically thick [O I] 63 μm emission, n_{H} of several 10^5 cm $^{-3}$, and temperatures $T_{\text{k}} \approx 200$ –400 K—thus compatible with the observed $T_{\text{p}}([\text{O I}]63 \mu\text{m})$ values (Sect. 4.2)—, typical of a dense PDR with a thermal pressure, P_{th}/k , of 10^7 to 10^8 K cm $^{-3}$. This agrees with previous observations of the large-scale PDRs at the surfaces of OMC-1 (Herrmann et al. 1997; Goicoechea et al. 2015b, 2019). An increase in velocity within the line wings (red and blue squares) is accompanied by a rise in the [O I] 63/145 line intensity ratio, consistent with higher gas densities and less opaque [O I] 63 μm emission. The lower $I_{145}(v)$ intensities as velocities increase simply reflect smaller $N(\text{O})$ column densities. Toward Peak 1, the [O I] 63 and 145 μm line-wing emission is consistent with n_{H} of several 10^5 to 10^6 cm $^{-3}$, $T_{\text{k}} \lesssim 500$ K, and $N(\text{O})$ of a few 10^{17} cm $^{-2}$. Fig. 8 also indicates that the postshock gas density is slightly lower in the blueshifted gas. When averaged over the entire outflow, the $I_{63}/I_{145}(v)$ ratio is highest at the largest velocities, where the H $_2$ and O column densities are lowest. The higher ratios imply n_{H} up to several 10^6 cm $^{-3}$, consistent with significant gas compression in the postshock gas.

6. Discussion

6.1. Peak 1 as a laboratory for shock modeling

Early models of Peak 1 have required two types of shocks to explain the observations (e.g., Chernoff et al. 1982; Draine & Roberge 1982; Neufeld & Dalgarno 1989; Haas et al. 1991; Kaufman & Neufeld 1996; Le Bourlot et al. 2002; Esplugues et al. 2014). The accepted picture was that a high-velocity molecular flow (the “plateau”) produces non-dissociative C-type shocks (with shock velocities $v_{\text{s}} \gtrsim 25$ km s $^{-1}$) as the flow interacts with the ambient molecular cloud, generating high temperatures (above 1000 K). These shocks lead to bright H $_2$ and high- J CO emission along with large H $_2\text{O}/\text{CO} > 1$ abundance ratios. Newer C-type shock models included the effects of modest external UV illumination (Melnick & Kaufman 2015) to explain the unusual detection of narrow-line O $_2$ toward Peak 1 (Chen et al. 2014). In addition, fast, $v_{\text{s}} = 70$ –80 km s $^{-1}$, dissociative, J-type shocks were

proposed to occur where a high-velocity wind impacts the expanding swept-up material (Hollenbach 1985), producing bright atomic fine-structure line emission. However, BN/KL’s explosive outflow is driven by bullets moving through the molecular cloud (e.g., Bally et al. 2015, 2020), rather than by stellar jets or winds, as in protostellar outflows. In Sect. 6.2 we explore the nature of the shocks driving the atomic fine-structure emission.

6.2. Nature of the [O I]–emitting shocks

Figure 9 compares the intensities of the [O I]63 μm , [O I]145 μm , and [C II]158 μm lines observed in the red and blue wings toward Peak 1 (Table 1) with those predicted by the Paris–Durham shock code⁶ (Godard et al. 2019) along the direction perpendicular (face-on) to the shock front. In this comparison, we assume an emission beam filling factor of $f = 1$. The model predictions are taken from Lehmann et al. (2022), which account for magnetized, molecular shocks with velocities in the range $v_S = 5\text{--}80\text{ km s}^{-1}$, preshock gas densities in the range $n_{\text{H},0} = 10^2\text{--}10^6\text{ cm}^{-3}$, and allow to include an external FUV radiation field (G_0^{ext}), in units of the Mathis field (Mathis et al. 1983).

The strength of the preshock magnetic field prior to the explosion is uncertain. Dust polarimetric observations of the plane-of-sky magnetic field in the quiescent cloud indicate values of a few hundred μG (Houde et al. 2009; Guerra et al. 2021), consistent with line-of-sight field strengths derived from CN Zeeman measurements (Crutcher et al. 1999; Crutcher 1999). Thus, all models in Fig. 9 adopt a reference magnetic parameter $b = 1$, where the preshock transverse magnetic field strength is given by $B = b(n_{\text{H},0}/\text{cm}^{-3})^{1/2}\text{ }\mu\text{G}$. For this range of parameters, shocks can be of type C , C^* , or CJ at $v_S < 25\text{ km s}^{-1}$, or J -type at $v_S > 25\text{ km s}^{-1}$ (Lehmann et al. 2020, 2022). The grid models assume either $G_0^{\text{ext}} = 0$ (left panels) or $G_0^{\text{ext}} = 10^3$ (right panels). Accurately determining the flux of external FUV photons reaching each bow-shock structure—whether locally self-generated, generated in nearby shocks, emitted by massive protostars within the region (BN, source I, and source n; Shuping et al. 2004), or originating from the Trapezium stars—is challenging, as it depends on both the porosity of the medium and the properties of the shocks and the protostars. The representative value of $G_0^{\text{ext}} = 10^3$ lies within the very rough estimates from FIR continuum observations toward Peak 1 (Goicoechea et al. 2015a).

In the absence of external irradiation ($G_0^{\text{ext}} = 0$), the predicted [O I] line intensities converge toward a plateau at high shock velocities, the level of which is primarily set by the preshock gas density, consistent with the dissociative shock models of Hollenbach & McKee (1989). Shocks with sufficiently high velocities generate a local FUV radiation field (e.g., Lehmann et al. 2020), whose intensity scales as

$$G_0^{\text{shock}} = 10^3 \left(\frac{n_{\text{H},0}}{10^4\text{ cm}^{-3}} \right) \left(\frac{v_S}{80\text{ km s}^{-1}} \right)^3, \quad (2)$$

for $30 < v_S \lesssim 100\text{ km s}^{-1}$ (Lehmann et al. 2020; Godard et al. 2024), and thus strongly depend on v_S . At low shock velocities, models with $G_0^{\text{ext}} = 0$ underpredict the observed [C II] 158 μm intensity by orders of magnitude. Marginally reproducing the [C II] 158 μm intensity would require very fast shocks, $v_S \gtrsim 80\text{ km s}^{-1}$. However, this is in contradiction with the Δv_{FWHM} and FWZI values of the observed fine-structure lines (Sect. 4.2), assuming that the flow is roughly directed along the line of sight. Therefore, a significant contribution from locally self-generated UV radiation is unlikely.

⁶ Available on the ISM platform <https://ism.obspm.fr>.

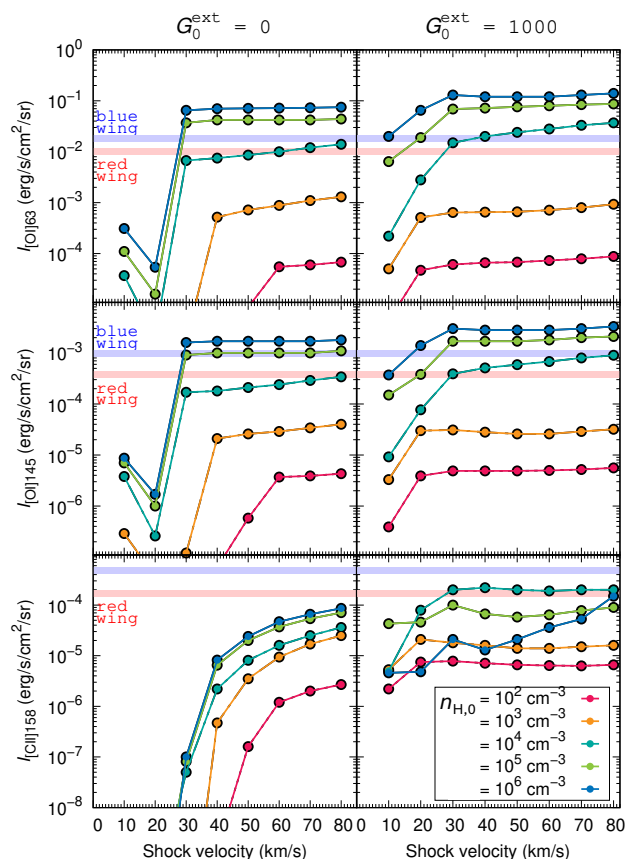


Fig. 9. FIR atomic line intensities as a function of shock velocity and preshock gas density (from Lehmann et al. 2022). The right panels show externally irradiated shocks. The horizontal blue and red lines indicate the observed line-wing intensities toward Peak 1 (Table 1).

External FUV radiation, which leads to atomic carbon photoionization and CO photodissociation, significantly enhances the intensities of atomic fine-structure lines (right panels of Fig. 9). Still, owing to the enhanced importance of C^+ recombination and chemical destruction at high gas densities, the [C II] 158 μm intensity does not increase monotonically with gas density.

Under external irradiation, the observations no longer constrain a unique set of shock parameters, but are instead consistent with a family of solutions involving J -type shocks with $v_S \simeq 30\text{--}40\text{ km s}^{-1}$ and $n_{\text{H},0} \gtrsim$ a few 10^4 cm^{-3} . Models with $G_0^{\text{ext}} = 10^3$ reproduce the [C II] 158 μm intensity of the redshifted wing, tracing gas moving into OMC-1, whereas the blueshifted wing emission, tracing gas moving toward the Trapezium, appears to require higher values of G_0^{ext} . In the following, we focus on the redshifted wing emission.

In these irradiated shocks, the predicted I_{63}/I_{158} line intensity ratio primarily scales with the preshock gas density and shows only a weak dependence on the shock velocity for $v_S > 30\text{ km s}^{-1}$ (see Fig. 10). The above family of solutions predicts $I_{63}/I_{158} \gtrsim 60$, consistent with the redshifted wing emission toward Peak 1, which shows intensity ratios up to $\sim 50\text{--}100$ (Fig. 7). Given the inferred postshock densities from the [O I] excitation analysis in Sect. 5.2, n_{H} of several 10^5 to 10^6 cm^{-3} , the resulting compression factors, $F = n_{\text{H}}/n_{\text{H},0} \gtrsim 30$, also support magnetized J -type shocks, where $F \sim v_S/b$ (Godard et al. 2024). The compressed magnetic field would have a strength of several mG, similar to the values observed toward BN/KL (Pattle et al. 2017; Guerra et al. 2021). All in all, the [O I] and [C II] line-wing emission is best reproduced by externally irradiated, dissociative

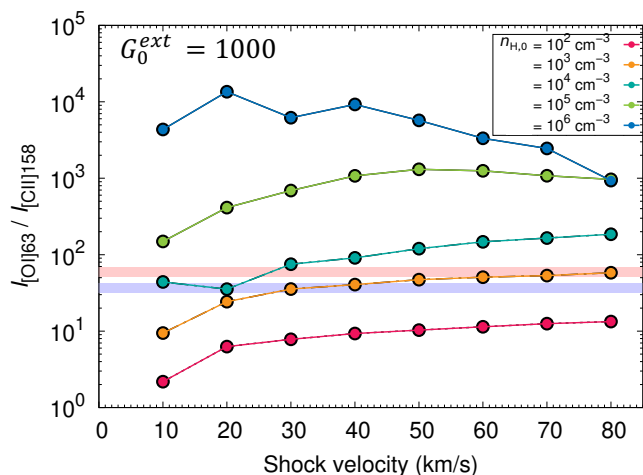


Fig. 10. [O I] 63 μm / [C II] 158 μm line intensity ratio as a function of shock velocity and preshock gas density in an externally irradiated shock with $G_0^{\text{ext}} = 10^3$ (from Lehmann et al. 2022). The horizontal blue and red lines indicate the observed line-wing intensities toward Peak 1.

J -type shocks with velocities of 30–40 km s⁻¹, preshock densities of a few 10⁴ cm⁻³, and compression factors consistent with postshock densities derived from the [O I] excitation analysis.

A more detailed interpretation would require to fully account for the geometry, time dependence, and spatial variations of b and G_0^{ext} across the outflow. Still, the results shown in Fig. 9 provide a general interpretative framework: dense bullets, with proper motions up to several hundred km s⁻¹, accelerated by the explosion event (i.e., Doi et al. 2002; Bally et al. 2015, 2017), interact with the ambient molecular cloud, generating bow-shock structures seen in [Fe II] knots and H₂ (Fig. 1). The highest bullet velocities exceed the observed FWZIs of the CO and OH lines, and imply molecular gas dissociation and the production of significant FUV radiation in many bow-shock tips (Eq. 2). Within this framework, surrounding fast shocks generate sufficient external FUV radiation to illuminate the inner layers of the bow-shock structures. The working surfaces of these bow shocks drive dissociative J -type shocks with velocities of a few tens of km s⁻¹, producing the observed [O I] emission.

Consistent with this scenario, the observed H I 21 cm line emission from atomic hydrogen—produced after H₂ (photo)dissociation—extends only up to $v_{\text{LSR}} \leq 31$ km s⁻¹ (see Fig. 20 of van der Werf et al. 2013) and broadly resembles the [O I] 63 μm emission, both in its spatial distribution and in its lack of the highest-velocity emission seen in CO or OH. The broader CO and OH line profiles indicate that the shocks responsible for their emission differ from those driving the atomic fine-structure emission. For instance, Melnick & Kaufman (2015) concluded that a C -shock with $v_S = 23$ km s⁻¹ propagating into a more shielded molecular clump (preshock density of 8×10^4 cm⁻³ and $G_0^{\text{ext}} = 1$) explains the detection of O₂ (Chen et al. 2014).

In our work, we conclude that, unlike earlier models (e.g., Hollenbach & McKee 1989; Haas et al. 1991), fast shocks with $v_S \approx 70$ –80 km s⁻¹ are not required to explain the observed atomic fine-structure line intensities and profiles. Instead, the observed lines are consistent with lower-velocity, dissociative J -type shocks illuminated by external FUV radiation, with $G_0^{\text{ext}} \approx 10^2$ – 10^3 , depending on the shock parameters (e.g., Kristensen et al. 2023). This radiation arises from surrounding fast shocks and possibly from nearby massive (proto)stars, including the Trapezium, enhancing the [C II] 158 μm emission, particularly in blueshifted gas moving toward the cluster.

Table 2. Total IR line luminosities in the BN/KL outflow region[†].

Line	Luminosity (L_{\odot})
[O I] 63 μm	$81.3 \pm 4.1^{a,b}$
[O I] 145 μm	$5.2 \pm 0.3^{a,b}$
[C II] 158 μm	$5.8 \pm 0.3^{a,b}$
H ₂ O (FIR and MIR)	35 ± 2^c
OH (FIR)	13 ± 1^c
CO (FIR and MIR)	$\sim 98 \pm 9^c$
H ₂ all lines	$\sim 120 \pm 60^d$
Total	$\sim 350^a$ (≥ 320 from the outflow ^b itself)

Notes. [†]Integrated over each full line profile. ^aExtracted over a 100'' × 80'' area (this work, box in Fig. 3). ^bIn Sect. 5.1 we determine that $\geq 65\%$, $\geq 50\%$, and $\geq 15\%$ of the observed [O I] 63 μm, [O I] 145 μm, and [C II] 158 μm line luminosity arises from the outflow and not from OMC-1’s face-on PDR. ^cFrom *Herschel* observations (Goicoechea et al. 2015a). ^dFrom ISO observations (Rosenthal et al. 2000).

6.3. Mass-Loss rate of the explosive outflow in Orion BN/KL

The energy loss from the outflow-driven shock provides a measure of the kinetic (mechanical) luminosity of the outflow, with $L_{\text{cool}} = (1 - f_m) L_{\text{kin}} = (1 - f_m) \frac{1}{2} \dot{M}_0 v_S^2$. In this expression⁷, L_{cool} is the total shock cooling rate and $(1 - f_m)$ denotes the fraction of the shock mechanical energy translated into internal excitation. In general, gas cooling proceeds through IR, H I, and optical line emission, $L_{\text{cool}} \approx L_{\text{IR}} + L_{\text{HI}} + L_{\text{optical}}$, where $L_{\text{IR}} = L_{\text{atoms}} + L_{\text{H}_2} + L_{\text{molec}}$ is the contribution from atomic fine-structure lines, H₂ lines, and other molecular lines (CO, H₂O, OH, etc.). L_{HI} and L_{optical} are only relevant in dissociative J -type shocks (Lehmann et al. 2020). L_{HI} represents the hydrogen-line cooling emission (e.g., Ly α , Ly β , and two-photon continuum) and L_{optical} refers to “optical” atomic forbidden-line emission, which arises from electronic transitions in the visible and NIR. From the above relation⁷,

$$\dot{M}_0 = 1.2 \cdot 10^{-2} \frac{(1 - f_m)^{-1}}{f_{\text{IR}}} \left(\frac{L_{\text{IR}}}{L_{\odot}} \right) \left(\frac{v_S}{\text{km s}^{-1}} \right)^{-2} M_{\odot} \text{ yr}^{-1}, \quad (3)$$

where f_{IR} is the fraction of the total cooling due to IR emission lines. In general, $f_{\text{IR}} \approx 0.5$ – 0.8 in C -type shocks (e.g., Kaufman et al. 1999; Karska et al. 2025) and $f_{\text{IR}} \approx 0.5$ in J -type shocks (e.g., Lehmann et al. 2020). Equation (3) has clear limitations when different types of shocks coexist, or when part of the emitted line luminosity arises from FUV-heated gas. In the following analysis, we assume that $v_S \approx 30$ – 40 km s⁻¹ represents the velocity range of the possible shock types in BN/KL’s outflow (if more than one), whether dissociative or non-dissociative. Table 2 summarizes the IR line luminosities, integrated over the entire profile, across the outflow (dashed square in Fig. 3). Inserting the outflow IR line luminosity, $L_{\text{IR}} \approx 320 L_{\odot}$, Eq. (3) yields a mass-loss rate of $\dot{M}_0 \approx (9.1 \pm 2.6) \times 10^{-3} M_{\odot} \text{ yr}^{-1}$, using $f_{\text{IR}} = 0.5$ (Fig. 3 of Lehmann et al. 2020) and $(1 - f_m) = 0.75$ (Kaufman & Neufeld 1996). Even if the derived \dot{M}_0 is an approximate value, the estimated mass-loss rate of BN/KL’s outflow is higher than that of steady protostellar outflows. Given a dynamical timescale of $t_{\text{dyn}} \approx 500$ yr (e.g., Zapata et al. 2009),

⁷ This equation is written in the reverse form compared to that used in some outflow papers (e.g., Maret et al. 2009), such that $L_{\text{kin}} \geq L_{\text{cool}}$.

Table 3. [O I] 63, 145 μm and FIR CO line luminosities toward the central emission (a size of ~ 0.2 pc) of several high-mass star-forming regions.

Source	L_{bol} (L_{\odot}) ^a	d (kpc) ^a	L_{OI} (L_{\odot})	$L_{\text{CO(PACS)}}$ (L_{\odot})	L_{CII} (L_{\odot})	$L_{\text{OI}}/L_{\text{bol}}$	$L_{\text{CO(PACS)}}/L_{\text{bol}}$	I_{63}/I_{158} (total line profile)
NGC7538-IRS1	1.1E+05	2.7	11 ^d	1.8 ^d	2.0 ^d	1.0E-04	1.6E-05	$\sim 5^d$
W3-IRS5	2.1E+05	2.0	4.2 ^d	10.5 ^d	1.5 ^e	2.0E-05	5.0E-05	$\sim 3^e$
DR21 (G81.7+0.6) [†]	1.3E+04	1.5	$\gtrsim 10^b$	1.2 ^d	2.5 ^b	$\gtrsim 7.7\text{E-}04$	9.2E-05	$\sim 5^b$
W28A (G5.89-0.39) [†]	4.1E+04	1.3	5.7 ^c	3.9 ^d	0.42 ^c	1.4E-04	9.5E-05	$\sim 13^c$
Orion BN/KL [†]	1.1E+05	0.4	86.5	64 ^f	5.8	7.9E-04	5.8E-04	~ 14 (map), ~ 23 (Peak 1)

Notes. [O I] 63, 145 μm , and [C II] 158 μm , and CO line luminosities for the small sample of massive sources observed with *Herschel*/PACS that exhibit clear [O I] 63 μm line emission spectra (Karska et al. 2014), that is, with little contribution from foreground absorption (Gerin et al. 2015). [†]Hosts an explosive outflow. ^aFrom van der Tak et al. (2013), Karska et al. (2014), and references therein. ^bEstimated from SOFIA/FIFI-LS (Karska et al. 2025). ^cFrom SOFIA/GREAT velocity-resolved observations (Leurini et al. 2015). ^dFrom PACS observations toward the central spaxel (Karska et al. 2014). ^eFrom PACS observations toward the central spaxel (Gerin et al. 2015). ^fFrom PACS maps (Goicoechea et al. 2015a).

the derived outflow mass is $M = t_{\text{dyn}} \dot{M}_0 \approx (3.3 - 5.9) M_{\odot}$. This estimate agrees with, yet may be more accurate than, mass estimates obtained from column densities computed under the LTE assumption (Snell et al. 1984; Peng et al. 2012). Still, future theoretical work should revisit the validity of Eq. (3) in the complex scenario described in Sect. 6.2, considering its dependence on multiple shocks and G_0^{ext} .

6.4. Mass-Loss rate from the putative BN outflow

Here, we assume that the spatially unresolved [O I] 63 μm emission detected around BN—both spatially and in LSR velocity (see Sect. 4.3)—arises from shocked gas produced by a compact outflow launched by this star. When [O I] 63 μm is the dominant gas coolant in a J -type “wind” shock—consistent with detection of this outflow only in [O I] 63 μm —Hollenbach (1985) showed that the line luminosity scales with the outflow mass-loss rate as $\dot{M} (M_{\odot} \text{yr}^{-1}) \approx 10^{-4} L_{63} (L_{\odot})$, provided that the flux of material into the shock satisfies $n_{\text{H},0} v_S \lesssim 10^{12} \text{cm}^{-2} \text{s}^{-1}$. In this regime, the particle flux is related to the [O I] 63 μm line intensity by $n_{\text{H},0} v_S \approx 10^{13} I_{63}$, with $n_{\text{H},0}$, v_S and I_{63} in cgs units.

The broad [O I] 63 μm line emission around BN shows $I_{63} \approx 5 \times 10^{-2} \text{erg s}^{-1} \text{cm}^{-2} \text{sr}^{-1}$ and $L_{63} \approx 0.6 L_{\odot}$ in $\lesssim 4000$ au. Thus, its contribution to the total L_{63} of the entire map is negligible. Using the relations above, we obtain, $n_{\text{H},0} v_S \approx 5 \times 10^{11} \text{cm}^{-2} \text{s}^{-1}$ and $\dot{M} \approx 6 \times 10^{-5} M_{\odot} \text{yr}^{-1}$, which is typical of accreting high-mass protostars (e.g., Beuther et al. 2002; Leurini et al. 2015). Assuming further that the shock velocity is comparable to the observed [O I] 63 μm line FWHM of the spectral component around BN, $\Delta v_{\text{FWHM}} \approx 15 \text{km s}^{-1}$ (Sect. 4.3), we derive a preshock gas density of several 10^5cm^{-3} . These results indicate that the kinematics, density, and mass-loss rate associated with the compact [O I] 63 μm emission around BN are consistent with a disk-accretion-driven outflow originating from BN. Further observations of additional tracers at high angular resolution will be needed to confirm the outflow versus wind bow shock scenario, or to constrain alternative interpretations.

6.5. Comparison with other high-mass star-forming regions

To investigate whether explosive outflows produce distinct spectroscopic features, in this section we compare the observed FIR [O I], [C II], and CO line luminosities of the BN/KL outflow with those measured in the central regions of other, more distant high-mass star-forming regions where similar observations have been carried out (e.g., Leurini et al. 2015). In the BN/KL outflow re-

gion, the FIR atomic line luminosity is dominated by [O I] 63 μm ⁸, which is ~ 15 times brighter than the [C II] 158 μm emission. The total [O I] 63 μm and 145 μm line luminosity is remarkably high, $86.5 L_{\odot}$, comparable to the total H_2 and CO luminosity (Rosenthal et al. 2000; Goicoechea et al. 2015a). This yields $L_{[\text{OI}]} / L_{\text{CO}} \approx 0.9$ and $L_{[\text{OI}]} / L_{\text{H}_2} \approx 0.7$. That is, about 25% of the total IR gas cooling is through [O I] emission lines (Table 2). Furthermore, the contribution to $L_{[\text{OI}]}$ from the broad spectral component, neglecting the narrow spike [O I] emission, is $55 L_{\odot}$.

Table 3 compares the FIR line luminosities toward the central regions of several high-mass star-forming regions, on scales of ~ 0.2 pc comparable to our BN/KL map. Interestingly, interferometric observations of the central regions of DR21 and G5.89–0.39 reveal CO outflows exhibiting fingers and Hubble-Lemaître flow kinematics, consistent with the presence of explosive outflows (e.g., Zapata et al. 2013, 2020; Guzmán Ccolque et al. 2024). These other regions exhibit fractional luminosities comparable to those of BN/KL outflow, both displaying high $L_{\text{OI}}/L_{\text{bol}}$ and $L_{\text{CO}}^{\text{FIR}}/L_{\text{bol}}$ ratios, $\gtrsim 10^{-4}$. In contrast, W3-IRS5, a proto-Trapezium system (e.g., Rodón et al. 2008), and NGC7538-IRS1, a massive star-forming core hosting an ultracompact H II region, a late O-to-early B star (Sandell & Sievers 2004), exhibit lower $L_{\text{OI}}/L_{\text{bol}}$ and $L_{\text{CO}}^{\text{FIR}}/L_{\text{bol}}$ luminosities. Pending more robust statistics, these high fractional luminosities may represent a distinctive signature of explosive outflows. Still, the BN/KL outflow stands out in FIR [O I] and CO line surface luminosities, per unit area, and the I_{63}/I_{158} intensity ratios exceed those in most regions, even when integrating over the full line profile, suggesting a denser gas environment.

7. Summary and conclusions

We presented velocity-resolved, sub-km s^{-1} -resolution maps of the [O I] 63 and 145 μm fine-structure emission lines along the wide-angle explosive outflow in Orion BN/KL. We complemented this data with new [C II] 158 μm and FIR OH line maps, all obtained with the GREAT heterodyne receivers on board SOFIA.

– We separated the quiescent (narrow [O I] line) and the outflow (broad [O I] line-wing) components, with the latter following the shock-excited H_2 emission, and the former primarily tracing the foreground, face-on PDR at the UV-illuminated rims of

⁸ Goicoechea et al. (2015a) derived $L_{[\text{OI}]} \approx 16 L_{\odot}$ from *Herschel*/PACS maps using a non-standard engineering observing mode to avoid saturation. This is a factor ~ 5 lower than the SOFIA/GREAT value. Although we do not find an obvious explanation for this discrepancy, the SOFIA luminosities are more consistent with KAO luminosities, $L_{[\text{OI}]} = 50 \pm 25 L_{\odot}$ (Werner et al. 1984).

OMC-1. The [O I] 63 μm line has a FWZI of $\sim 85 \text{ km s}^{-1}$. The FWZI of the [C II] 158 μm line is smaller, $\leq 50 \text{ km s}^{-1}$, implying that the highest-velocity gas either lacks FUV illumination or that, more likely, C^+ is quickly converted into other species.

– The broad [O I] 145 μm component ($\Delta v_{\text{FWHM}} \approx 20 \text{ km s}^{-1}$) is narrower than the corresponding CO and OH emission ($\Delta v_{\text{FWHM}} \gtrsim 30 \text{ km s}^{-1}$), which also exhibit larger FWZIs ($\gtrsim 150 \text{ km s}^{-1}$). This suggests that the shocks producing the [O I] emission differ either in nature or in exact location from those driving the highest-velocity CO and OH emission.

– The [O I] 63/145 and [O I] 63/[C II] 158 intensity ratios attain remarkably high values in the line wings (20–30 and 40–60, respectively), exceeding those observed in PDRs and typical protostellar outflows. They are consistent with dense ($n_{\text{H}} \gtrsim 10^5\text{--}10^6 \text{ cm}^{-3}$) and warm ($T \lesssim 500 \text{ K}$) postshock gas.

– The fine-structure line-wing emission is consistent with originating in externally irradiated, magnetized, dissociative J -type shocks with $v_{\text{S}} \approx 30\text{--}40 \text{ km s}^{-1}$ and preshock densities of a few 10^4 cm^{-3} . External FUV radiation arises from surrounding fast shocks and possibly from massive (proto)stars in the region if the medium is sufficiently porous.

– The [O I] 63 and 145 μm luminosity along the outflow region is significantly high, amounting to $86.5 L_{\odot}$, with $55 L_{\odot}$ contributed by the broad component alone. This is comparable to the H_2 and CO line luminosities, yielding $L_{[\text{O I}]} / L_{\text{CO}} \approx 0.9$ and $L_{[\text{O I}]} / L_{\text{H}_2} \approx 0.7$. These values imply an outflow mass-loss rate of $(9.1 \pm 2.6) \times 10^{-3} M_{\odot} \text{ yr}^{-1}$ and a mass of $M \approx (3.3\text{--}5.9) M_{\odot}$.

– We report the detection of spatially unresolved, broad [O I] 63 μm emission, slightly offset from BN but aligned with the direction of the star's proper motion. This $L_{63} \approx 0.6 L_{\odot}$ emission may arise from an unresolved outflow (corresponding to a mass-loss rate of several $10^{-5} M_{\odot} \text{ yr}^{-1}$) or a wind bow shock produced by the supersonic motion of this wind-blowing runaway B star.

The FIR [C II] and [O I] line intensities, among the brightest tracers of interstellar shocks and PDRs, probe the thermal budget and the presence of FUV radiation, while sub- km s^{-1} -resolution maps reveal the gas dynamics, allowing us to quantify the contributions of radiative and mechanical feedback. Unfortunately, following the end of SOFIA operations, very high-spectral-resolution mapping has been performed for only a few regions of the sky. A FIR heterodyne mission (airborne or space) would be the only telescope to provide this essential missing information.

Acknowledgements. We thank our referee for a constructive report that allowed us to improve the presentation of our work. This work is based on observations made with SOFIA (NASA/DLR). SOFIA was jointly operated by the Universities Space Research Association, Inc. (USRA), under NASA contract NAS2-97001, and the Deutsches SOFIA Institut (DSI) under the DLR contract 50 OK 0901 and 50 OK 1301 to the University of Stuttgart. GREAT was a development by the MPI für Radioastronomie and the KOSMA/Universität zu Köln, in cooperation with the DLR Institut für Optische Sensorsysteme. GREAT development was financed by the participating institutes, by DLR under Grants 50 OK 1102, 1103, and 1104, and within the Collaborative Research Centre 956, funded by the Deutsche Forschungsgemeinschaft (DFG). JRG, MGSM, and MZ thank the Spanish MICIU for funding support under grant PID2023-146667NB-I00. MZ acknowledges the JdC Postdoctoral Fellowship JDC2024-054658-I, funded by MICIU/AEI/10.13039/501100011033 and by the ESF+. BG and AG acknowledge the support from the Programme National “Physique et Chimie du Milieu Interstellaire” (PCMI) of CNRS/INSU with INC/INP funded by CEA and CNES.

References

Allen, D. A. & Burton, M. G. 1993, *Nature*, 363, 54
 Bally, J. 2008, *Overview of the Orion Complex*, ed. B. Reipurth, 459
 Bally, J., Cunningham, N. J., Moeckel, N., et al. 2011, *ApJ*, 727, 113
 Bally, J., Ginsburg, A., Arce, H., et al. 2017, *ApJ*, 837, 60
 Bally, J., Ginsburg, A., Forbrich, J., & Vargas-González, J. 2020, *ApJ*, 889, 178

Bally, J., Ginsburg, A., Silvia, D., & Youngblood, A. 2015, *A&A*, 579, A130
 Bally, J., Langer, W. D., Stark, A. A., & Wilson, R. W. 1987, *ApJ*, 312, L45
 Bally, J. & Zinnecker, H. 2005, *AJ*, 129, 2281
 Baranov, V. B., Krasnobaev, K. V., & Kulikovskii, A. G. 1971, *Soviet Physics Doklady*, 15, 791
 Beckwith, S., Persson, S. E., Neugebauer, G., & Becklin, E. E. 1978, *ApJ*, 223, 464
 Bernard-Salas, J., Habart, E., Arab, H., et al. 2012, *A&A*, 538, A37
 Berné, O., Marcelino, N., & Cernicharo, J. 2014, *ApJ*, 795, 13
 Betz, A. L. & Boreiko, R. T. 1989, *ApJ*, 346, L101
 Beuther, H., Linz, H., Bik, A., Goto, M., & Henning, T. 2010, *A&A*, 512, A29
 Beuther, H. & Nissen, H. D. 2008, *ApJ*, 679, L121
 Beuther, H., Schilke, P., Sridharan, T. K., et al. 2002, *A&A*, 383, 892
 Blake, G. A., Sutton, E. C., Masson, C. R., & Phillips, T. G. 1987, *ApJ*, 315, 621
 Cernicharo, J., Goicoechea, J. R., Daniel, F., et al. 2006, *ApJ*, 649, L33
 Chen, J.-H., Goldsmith, P. F., Viti, S., et al. 2014, *ApJ*, 793, 111
 Chernoff, D. F., Hollenbach, D. J., & McKee, C. F. 1982, *ApJ*, 259, L97
 Crutcher, R. M. 1999, *ApJ*, 520, 706
 Crutcher, R. M., Troland, T. H., Lazareff, B., Paubert, G., & Kazès, I. 1999, *ApJ*, 514, L121
 Doi, T., O’Dell, C. R., & Hartigan, P. 2002, *AJ*, 124, 445
 Draine, B. T. 1980, *ApJ*, 241, 1021
 Draine, B. T. & Roberge, W. G. 1982, *ApJ*, 259, L91
 Duran, C. A., Gusten, R., Risacher, C., et al. 2021, *IEEE Transactions on Terahertz Science and Technology*, 11, 194
 Elitzur, M. & Asensio Ramos, A. 2006, *MNRAS*, 365, 779
 Esplugues, G. B., Viti, S., Goicoechea, J. R., & Cernicharo, J. 2014, *A&A*, 567, A95
 Geballe, T. R., Burton, M. G., & Pike, R. E. 2017, *ApJ*, 837, 83
 Genzel, R., Reid, M. J., Moran, J. M., & Downes, D. 1981, *ApJ*, 244, 884
 Genzel, R. & Stutzki, J. 1989, *ARA&A*, 27, 41
 Gerin, M., Ruaud, M., Goicoechea, J. R., et al. 2015, *A&A*, 573, A30
 Godard, B., des Forêts, G. P., & Bialy, S. 2024, *A&A*, 688, A169
 Godard, B., Pineau des Forêts, G., Lesaffre, P., et al. 2019, *A&A*, 622, A100
 Goddi, C., Humphreys, E. M. L., Greenhill, L. J., Chandler, C. J., & Matthews, L. D. 2011, *ApJ*, 728, 15
 Goicoechea, J. R. & Cernicharo, J. 2002, *ApJ*, 576, L77
 Goicoechea, J. R., Cernicharo, J., Lerate, M. R., et al. 2006a, *ApJ*, 641, L49
 Goicoechea, J. R., Chavarría, L., Cernicharo, J., et al. 2015a, *ApJ*, 799, 102
 Goicoechea, J. R., Compiègne, M., & Habart, E. 2009, *ApJ*, 699, L165
 Goicoechea, J. R., Pety, J., Gerin, M., et al. 2006b, *A&A*, 456, 565
 Goicoechea, J. R., Santa-Maria, M. G., Bron, E., et al. 2019, *A&A*, 622, A91
 Goicoechea, J. R., Teysier, D., Etxaluz, M., et al. 2015b, *ApJ*, 812, 75
 Goldsmith, P. F. 2019, *ApJ*, 887, 54
 Gómez, L., Rodríguez, L. F., Loinard, L., et al. 2008, *ApJ*, 685, 333
 Gómez, L., Rodríguez, L. F., Loinard, L., et al. 2005, *ApJ*, 635, 1166
 González-Alfonso, E., Wright, C. M., Cernicharo, J., et al. 2002, *A&A*, 386, 1074
 Guan, X., Stutzki, J., Graf, U. U., et al. 2012, *A&A*, 542, L4
 Guerra, J. A., Chuss, D. T., Dowell, C. D., et al. 2021, *ApJ*, 908, 98
 Guzmán Colque, E., Fernández López, M., Zapata, L. A., Bally, J., & Rivera-Ortiz, P. R. 2024, *A&A*, 689, A339
 Haas, M. R., Hollenbach, D., & Erickson, E. F. 1991, *ApJ*, 374, 555
 Habart, E., Peeters, E., Berné, O., et al. 2024, *A&A*, 685, A73
 Herrmann, F., Madden, S. C., Nikola, T., et al. 1997, *ApJ*, 481, 343
 Heyminck, S., Graf, U. U., Güsten, R., et al. 2012, *A&A*, 542, L1
 Hollenbach, D. 1985, *Icarus*, 61, 36
 Hollenbach, D. & McKee, C. F. 1979, *ApJS*, 41, 555
 Hollenbach, D. & McKee, C. F. 1989, *ApJ*, 342, 306
 Houde, M., Vaillancourt, J. E., Hildebrand, R. H., Chitsazzadeh, S., & Kirby, L. 2009, *ApJ*, 706, 1504
 Jiang, Z., Tamura, M., Fukagawa, M., et al. 2005, *Nature*, 437, 112
 Joblin, C., Bron, E., Pinto, C., et al. 2018, *A&A*, 615, A129
 Karska, A., Figueira, M., Mirocha, A., et al. 2025, *A&A*, 697, A186
 Karska, A., Herpin, F., Bruderer, S., et al. 2014, *A&A*, 562, A45
 Kaufman, M. J. & Neufeld, D. A. 1996, *ApJ*, 456, 611
 Kaufman, M. J., Wolfire, M. G., Hollenbach, D. J., & Luhman, M. L. 1999, *ApJ*, 527, 795
 Kavak, Ü., Goicoechea, J. R., Pabst, C. H. M., et al. 2022, *A&A*, 660, A109
 Klein, B., Hochgürtel, S., Krämer, I., et al. 2012, *A&A*, 542, L3
 Kristensen, L. E., Godard, B., Guillard, P., Gusdorf, A., & Pineau des Forêts, G. 2023, *A&A*, 675, A86
 Kristensen, L. E., Ravkilde, T. L., Field, D., Lemaire, J. L., & Pineau Des Forêts, G. 2007, *A&A*, 469, 561
 Kristensen, L. E., Ravkilde, T. L., Pineau Des Forêts, G., et al. 2008, *A&A*, 477, 203
 Kwan, J. & Scoville, N. 1976, *ApJ*, 210, L39
 Le Bourlot, J., Pineau des Forêts, G., Flower, D. R., & Cabrit, S. 2002, *MNRAS*, 332, 985
 Lehmann, A., Godard, B., Pineau des Forêts, G., & Falgarone, E. 2020, *A&A*, 643, A101

- Lehmann, A., Godard, B., Pineau des Forêts, G., Vidal-García, A., & Falgarone, E. 2022, *A&A*, 658, A165
- Lerate, M. R., Barlow, M. J., Swinyard, B. M., et al. 2006, *MNRAS*, 370, 597
- Lesaffre, P., Pineau des Forêts, G., Godard, B., et al. 2013, *A&A*, 550, A106
- Leurini, S., Wyrowski, F., Wiesemeyer, H., et al. 2015, *A&A*, 584, A70
- Lique, F., Klos, J., Alexander, M. H., Le Picard, S. D., & Dagdigan, P. J. 2018, *MNRAS*, 474, 2313
- Liseau, R., Justtanont, K., & Tielens, A. G. G. M. 2006, *A&A*, 446, 561
- Lonsdale, C. J., Becklin, E. E., Lee, T. J., & Stewart, J. M. 1982, *AJ*, 87, 1819
- Maret, S., Bergin, E. A., Neufeld, D. A., et al. 2009, *ApJ*, 698, 1244
- Mathis, J. S., Mezger, P. G., & Panagia, N. 1983, *A&A*, 128, 212
- McCaughrean, M. J. & Mac Low, M.-M. 1997, *AJ*, 113, 391
- McCaughrean, M. J. & Pearson, S. G. 2023, arXiv e-prints, arXiv:2310.03552
- Melnick, G. J., Genzel, R., & Lugten, J. B. 1987, *ApJ*, 321, 530
- Melnick, G. J. & Kaufman, M. J. 2015, *ApJ*, 806, 227
- Melnick, G. J., Stacey, G. J., Genzel, R., Lugten, J. B., & Poglitsch, A. 1990, *ApJ*, 348, 161
- Menten, K. M. & Reid, M. J. 1995, *ApJ*, 445, L157
- Menten, K. M., Reid, M. J., Forbrich, J., & Brunthaler, A. 2007, *A&A*, 474, 515
- Monteiro, T. S. & Flower, D. R. 1987, *MNRAS*, 228, 101
- Morris, P. W., Gupta, H., Nagy, Z., et al. 2016, *ApJ*, 829, 15
- Neufeld, D. A. & Dalgarno, A. 1989, *ApJ*, 344, 251
- Nissen, H. D., Cunningham, N. J., Gustafsson, M., et al. 2012, *A&A*, 540, A119
- O'Dell, C. R. 2001, *ARA&A*, 39, 99
- O'Dell, C. R., Ferland, G. J., Henney, W. J., et al. 2015, *AJ*, 150, 108
- Pabst, C., Higgins, R., Goicoechea, J. R., et al. 2019, *Nature*, 565, 618
- Pabst, C. H. M., Goicoechea, J. R., Teyssier, D., et al. 2020, *A&A*, 639, A2
- Pattle, K., Ward-Thompson, D., Berry, D., et al. 2017, *ApJ*, 846, 122
- Peng, T.-C., Wyrowski, F., Zapata, L. A., Güsten, R., & Menten, K. M. 2012, *A&A*, 538, A12
- Plambeck, R. L., Bolatto, A. D., Carpenter, J. M., et al. 2013, *ApJ*, 765, 40
- Plambeck, R. L., Wright, M. C. H., Welch, W. J., et al. 1982, *ApJ*, 259, 617
- Risacher, C., Güsten, R., Stutzki, J., et al. 2018, *Journal of Astronomical Instrumentation*, 7, 1840014
- Risacher, C., Güsten, R., Stutzki, J., et al. 2016a, *A&A*, 595, A34
- Risacher, C., Güsten, R., Stutzki, J., et al. 2016b, *IEEE Transactions on Terahertz Science and Technology*, 6, 199
- Rodón, J. A., Beuther, H., Megeath, S. T., & van der Tak, F. F. S. 2008, *A&A*, 490, 213
- Rodríguez, L. F., Poveda, A., Lizano, S., & Allen, C. 2005, *ApJ*, 627, L65
- Rosenthal, D., Bertoldi, F., & Drapatz, S. 2000, *A&A*, 356, 705
- Sandell, G. & Sievers, A. 2004, *ApJ*, 600, 269
- Schöier, F. L., van der Tak, F. F. S., van Dishoeck, E. F., & Black, J. H. 2005, *A&A*, 432, 369
- Scoville, N., Kleinmann, S. G., Hall, D. N. B., & Ridgway, S. T. 1983, *ApJ*, 275, 201
- Shuping, R. Y., Morris, M., & Bally, J. 2004, *AJ*, 128, 363
- Snell, R. L., Scoville, N. Z., Sanders, D. B., & Erickson, N. R. 1984, *ApJ*, 284, 176
- Stacey, G. J., Jaffe, D. T., Geis, N., et al. 1993, *ApJ*, 404, 219
- Tan, J. C. 2004, *ApJ*, 607, L47
- Tercero, B., Cernicharo, J., Pardo, J. R., & Goicoechea, J. R. 2010, *A&A*, 517, A96
- Tielens, A. G. G. M. & Hollenbach, D. 1985, *ApJ*, 291, 747
- van der Tak, F. F. S., Chavarría, L., Herpin, F., et al. 2013, *A&A*, 554, A83
- van der Werf, P. P., Goss, W. M., & O'Dell, C. R. 2013, *ApJ*, 762, 101
- Werner, M. W., Crawford, M. K., Genzel, R., et al. 1984, *ApJ*, 282, L81
- Werner, M. W., Gatley, I., Harper, D. A., et al. 1976, *ApJ*, 204, 420
- Wilkin, F. P. 1996, *ApJ*, 459, L31
- Wright, M., Bally, J., Hirota, T., et al. 2022, *ApJ*, 924, 107
- Young, E. T., Becklin, E. E., Marcum, P. M., et al. 2012, *ApJ*, 749, L17
- Youngblood, A., France, K., Ginsburg, A., Hoadley, K., & Bally, J. 2018, *ApJ*, 857, 7
- Zapata, L. A., Fernández-López, M., Leurini, S., et al. 2023, *ApJ*, 956, L35
- Zapata, L. A., Ho, P. T. P., Fernández-López, M., et al. 2020, *ApJ*, 902, L47
- Zapata, L. A., Schmid-Burgk, J., Ho, P. T. P., Rodríguez, L. F., & Menten, K. M. 2009, *ApJ*, 704, L45
- Zapata, L. A., Schmid-Burgk, J., Pérez-Goytia, N., et al. 2013, *ApJ*, 765, L29

Table A.1. Observed lines, instrument configurations and observing modes.

Cycle	Date	Config.	Transition (λ_0)	ν_0 (GHz)	θ_{mb} ($''$)	E_{up} (K)	n_{crit} (cm^{-3})	Instrument	Obs.Mode	Map Coverage $\Delta R.A. \times \Delta Dec.$ ($'' \times ''$)
9	23.11.21	LFA-H	[C II] $^2P_{3/2} - ^2P_{1/2}$	1900.53690 (L)	14.8	91	6×10^3	upGREAT	TP OTF	144×123 by 3 $''$
9	19.11.21	LFA-H	(157.7 μm)							
8	09.03.21	LFA-H		1900.53690 (U)						
8	24.02.21	LFA-H								
4	08.11.16	LFA-V	OH $^2\Pi_{1/2} J=3/2-1/2$	1834.74615 (U)	14.6	268	$> 10^9$	upGREAT	Ch OTF	108×84 by 6 $''$
4	09.11.16	LFA-V	(163.4 μm)							
8	11.02.21	4G-4	OH $^2\Pi_{3/2} J=5/2-3/2$	2514.32943 (L)	11.3	120	5×10^8	4GREAT	Ch Ras	24×24 by 6 $''$
1	31.01.14	M	(119.2 μm)	2514.32943 (U)				GREAT	Ch Ras	40×40 by 10 $''$
8	09.03.21	LFA-V	[O I] $^3P_0 - ^3P_1$	2060.06886 (U)	12.9	327	6×10^6	upGREAT	TP OTF	144×123 by 3 $''$
8	24.02.21	LFA-V	(145.6 μm)							
9	23.11.21	HFA-V	[O I] $^3P_1 - ^3P_2$	4744.77749 (L)	6.3	228	5×10^5	upGREAT	TP OTF	144×123 by 3 $''$
9	19.11.21	HFA-V	(63.2 μm)							
8	09.03.21	HFA-V								
8	24.02.21	HFA-V								

Notes. For each of the transitions studied in this work, here we quote the SOFIA observing cycle, the UT date of the observation and the instrument configuration. Rest frequencies (in parenthesis, the sideband used for the LO tuning), upper level energies above ground and characteristic critical densities are adopted and calculated from the Leiden Atomic and Molecular Database, LAMDA (Schöier et al. 2005). During observing cycle 1 single-pixel GREAT channels were operated (Heyminck et al. 2012); since cycle 4 the dual-color upGREAT array spectrometers were operated, which made it possible to record up to three different frequencies simultaneously (for details, see Risacher et al. (2016b), Risacher et al. (2016a), Risacher et al. (2018)). In 2021 the multi-color 4GREAT was added to the suite of GREAT flight configurations (Duran et al. 2021). Half-power beam width are quoted from these publications.

The observing modes are indicated: total power (TP) or chopped (ch) on-the-fly (OTF: data is acquired while slewing the telescope), or raster mode (the telescope stays pointed while integrating). The size of a given map is quoted for the central array pixel only; the step between dumps (along the scanning direction) and between adjacent OTF slews is given or the grid used for pointed raster observations.

Appendix A: Observed lines, instrument configurations and observing modes.

Table A.1 summarizes the instrument configurations, observing parameters, and observed FIR line properties.

Appendix B: Complementary observational figures

This Appendix presents additional figures that aim to better understand the velocity structure of BN/KL outflow.

Appendix B.1: Velocity channel maps

Figure B.1 shows velocity-channel maps (in K km s^{-1} units) of the FIR lines observed with SOFIA and the CO $J = 10-9$ line observed with *Herschel*/HIFI (Goicoechea et al. 2019).

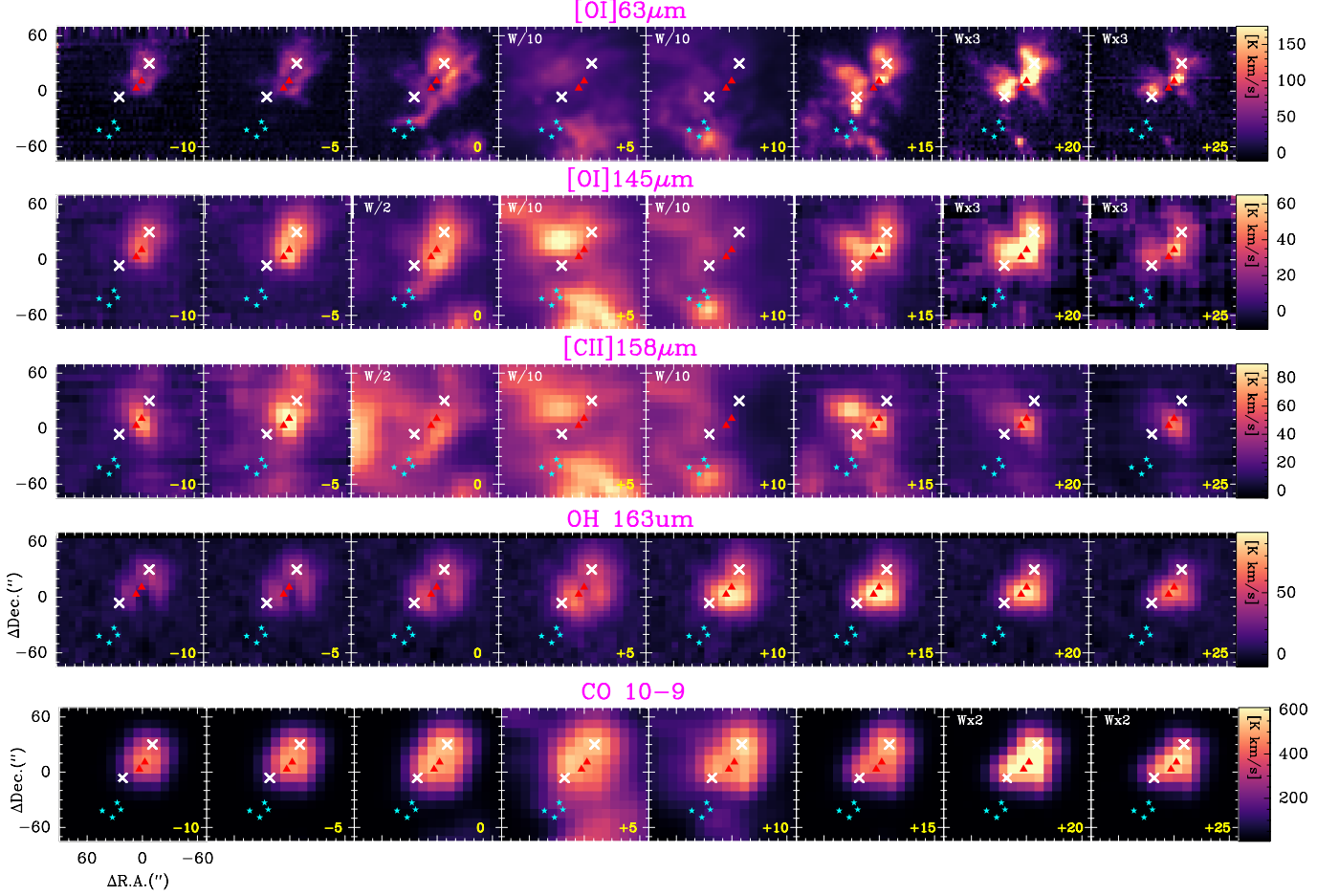


Fig. B.1. Velocity channel maps at their native angular resolution and in K km s^{-1} intensity units, from $v_{\text{LSR}} = -10$ to $+25 \text{ km s}^{-1}$ in bins of 5 km s^{-1} [$v, v + 5$], with v indicated in the bottom-right corner of each panel. The map at $v = +5 \text{ km s}^{-1}$ shows the emission at the systemic velocity of the quiescent gas in OMC-1, $v_{\text{LSR},0} \approx 8-9 \text{ km s}^{-1}$, dominated by extended emission from a face-on PDR. The main reference positions discussed in the text are illustrated with symbols (see Fig. 2).

Figure B.2 shows channel maps of line intensity ratios for the different FIR atomic lines (with intensities in cgs units).

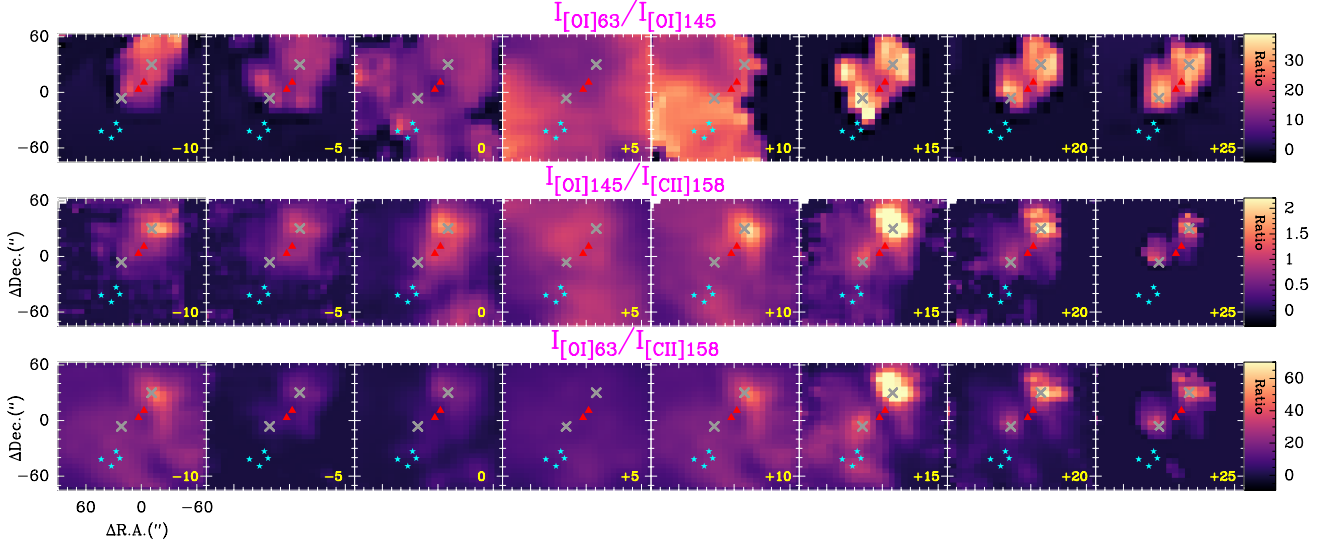


Fig. B.2. Velocity-resolved line intensity ratio channel maps (same velocity bins as in Fig. B.1) convolved at a common angular resolution of $15''$, with the integrated line intensities in $\text{erg s}^{-1} \text{cm}^{-2} \text{sr}^{-1}$. The map at $v = +5 \text{ km s}^{-1}$ shows the emission at the systemic velocity of the quiescent gas.

Appendix B.2: Line profiles toward the FIR continuum peak

Figure B.3 (right panel) shows a zoom on the low-intensity features of several FIR lines toward the FIR continuum peak position (the hot core region), with the main [O I] $63 \mu\text{m}$ absorption and [C II] $158 \mu\text{m}$ emission features labelled.

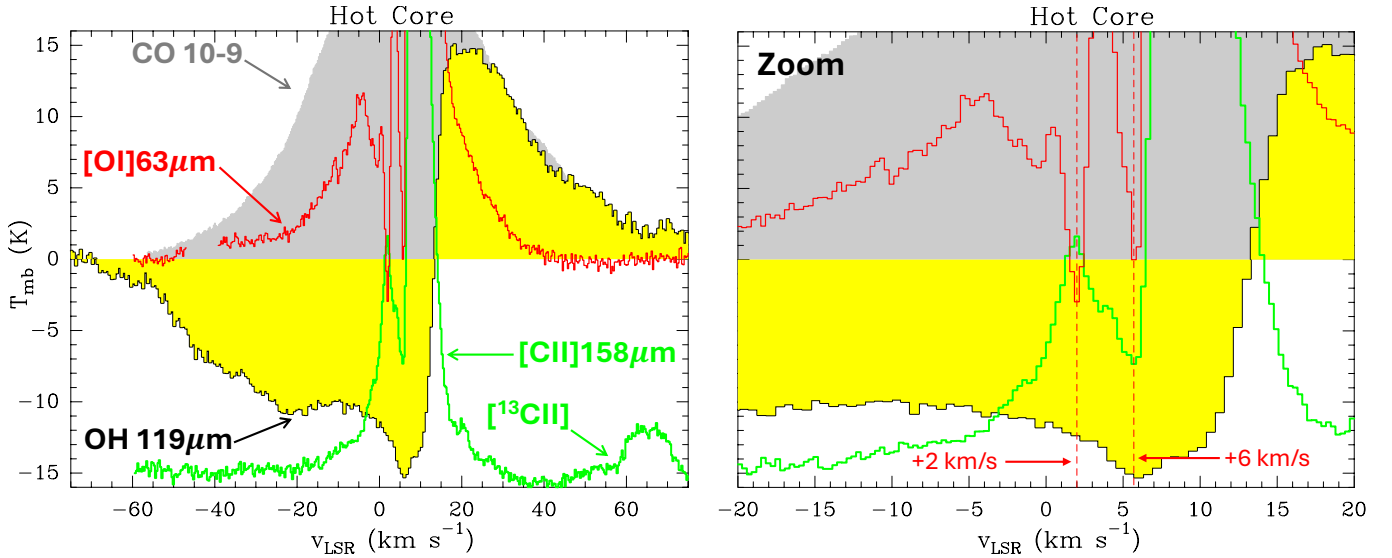


Fig. B.3. OH $119 \mu\text{m}$ P-Cygni profile toward the hot core (FIR continuum peak), compared to other line profiles. The OH $119 \mu\text{m}$ absorption dip agrees with [O I] $63 \mu\text{m}$ absorption at $+6 \text{ km s}^{-1}$ (hot core velocities). The [C II] $158 \mu\text{m}$ emission and [O I] $63 \mu\text{m}$ absorption at $+2 \text{ km s}^{-1}$ corresponds to a gas structure in the foreground.

Appendix C: Nonlocal, non-LTE [O I] radiative transfer models

In our [O I] excitation and radiative transfer models (Goicoechea et al. 2006b, 2009), we adopted the fine-structure O–H₂ and O–H collisional rate coefficients calculated by Lique et al. (2018) in the 10–1000 K temperature range. As observed, the FIR [O I] fine-structure line emission in the outflow arises from molecular gas with some atomic H (van der Werf et al. 2013). Hence, we define the gas density as $n_{\text{H}} = n(\text{H}) + 2n(\text{H}_2)$, and adopted $n(\text{H}_2)/n(\text{H}) \simeq 4$ in the models. We verified that this choice does not affect our main conclusions and results. We ran spherical models with uniform gas densities ($n_{\text{H}} = 10^4$ – 10^8 cm^{-3}), temperatures ($T_{\text{k}} = 200$ and 500 K , based on the observed $T_{\text{mb}}([\text{O I}] 63 \mu\text{m})$ line peaks), and a fixed velocity dispersion, $\sigma_{\text{turb}} = 8.5 \text{ km s}^{-1}$ (i.e., $\Delta v_{\text{turb,FWHM}} \simeq 20 \text{ km s}^{-1}$), matching the observed [O I] 145 μm broad component toward Peak 1.

Figure C.1 shows the results of the grid, displaying I_{145} as a function of n_{H} (left panels) for different atomic oxygen column densities: 2×10^{17} , 2×10^{18} , and $2 \times 10^{19} \text{ cm}^{-2}$, and gas temperatures. The right panels show the resulting I_{63}/I_{145} line intensity ratio as a function of n_{H} . Continuous curves refer to models without external FIR illumination. The red and cyan colored areas show the I_{63}/I_{145} ratios measured toward Peak 1 in the red- and blue-shifted wings, respectively (extracted from Table 1). These ratios are consistent with the presence of dense ($n_{\text{H}} \simeq$ several 10^5 to 10^6 cm^{-3}) and warm ($T \lesssim 500 \text{ K}$) postshock gas, with $N(\text{O}) \simeq$ a few 10^{18} cm^{-2} .

In these plots, the opacity of the [O I] 63 μm line increases as $N(\text{O})$ increases, from optically thin to thick emission. That is, from high to low densities—from right to left in the figures—as collisional excitation becomes less important and the low energy levels become more populated. This is reflected in very subthermal [O I] 63 μm excitation ($T_{\text{ex},63\mu\text{m}} \ll T_{\text{k}}$) when $n_{\text{H}} \ll n_{\text{cr},63\mu\text{m}}$ (Fig. C.2, left panels). Figure C.2 shows the average $T_{\text{ex},63\mu\text{m}}$ and $T_{\text{ex},145\mu\text{m}}$ in the models, but we note that due to radiative transfer effects—such as line trapping—the local T_{ex} values vary with position, even under uniform physical conditions. The excitation of the [O I] 145 μm line is more complex and is governed by the spontaneous radiative decay of the upper level ($^3\text{P}_0$), which is roughly five times lower than that of the lower level ($^3\text{P}_1$). In addition, the collisional de-excitation rate coefficient for O–H₂ collisions of the $^3\text{P}_0$ – $^3\text{P}_1$ (145 μm) transition is significantly smaller than that of the $^3\text{P}_1$ – $^3\text{P}_2$ (63 μm) transition (e.g., Monteiro & Flower 1987; Lique et al. 2018). These properties lead to [O I] 145 μm population inversions ($T_{\text{ex},145\mu\text{m}} < 0 \text{ K}$) at low densities ($n_{\text{H}} < n_{\text{cr},145\mu\text{m}}$) and suprathermal emission ($T_{\text{ex},145\mu\text{m}} > T_{\text{k}}$) at high densities (previously discussed by Liseau et al. 2006; Elitzur & Asensio Ramos 2006; Goicoechea et al. 2009; Goldsmith 2019). These features are evident in the right panels of Fig. C.2.

To investigate the role of FIR pumping in the [O I] excitation, the dotted curves in Figs. C.2 and C.1 represent the same models but adding external FIR continuum illumination. We model the continuum background as the sum of the cosmic microwave background and a modified blackbody, $\eta B(T_{\text{d}})(1 - \exp(-\tau_{\text{d},\lambda}))$, at a dust color temperature of $T_{\text{d}} = 100 \text{ K}$. In this expression, η is the filling factor of the background FIR continuum emission, which we set to 0.5. The dust continuum emission is assumed to be optically thick at 100 μm , with $\tau_{\text{d},\lambda} = 7 [100/\lambda(\mu\text{m})]^2$, and represents the typical FIR dust continuum emission close to the hot core region (see Goicoechea et al. 2015a). The main role of this FIR continuum is to produce [O I] 63 μm line absorption (when $T_{\text{ex}} < T_{\text{cont}}$) at low gas densities, n_{H} below a few 10^4 cm^{-3} , as the [O I] 63 μm line becomes optically thick, for $N(\text{O}) \gtrsim 10^{18} \text{ cm}^{-2}$.

In general, FIR pumping increases the population of the $^3\text{P}_1$ level (in this case increasing the excitation temperature of the [O I] 63 μm line; see dotted curves in Fig. C.2, left), thereby reducing the population inversion of the $^3\text{P}_0$ – $^3\text{P}_1$ transition at [O I] 145 μm . At low to moderate gas densities, the [O I] 63 μm line intensity decreases, whereas the intensity of the [O I] 145 μm remains nearly unchanged. Consequently, the I_{63}/I_{145} intensity ratio is slightly lower (dotted curves in Fig. C.1, right) than in the non-illuminated case. Hence, the inferred postshock gas density may be slightly higher.

At high densities, however, the main effect of FIR pumping is to slightly reduce $T_{\text{ex},145\mu\text{m}}$, although it remains suprathermal (Fig. C.2, right), leading to a slightly higher I_{63}/I_{145} intensity ratio (Fig. C.1, right).

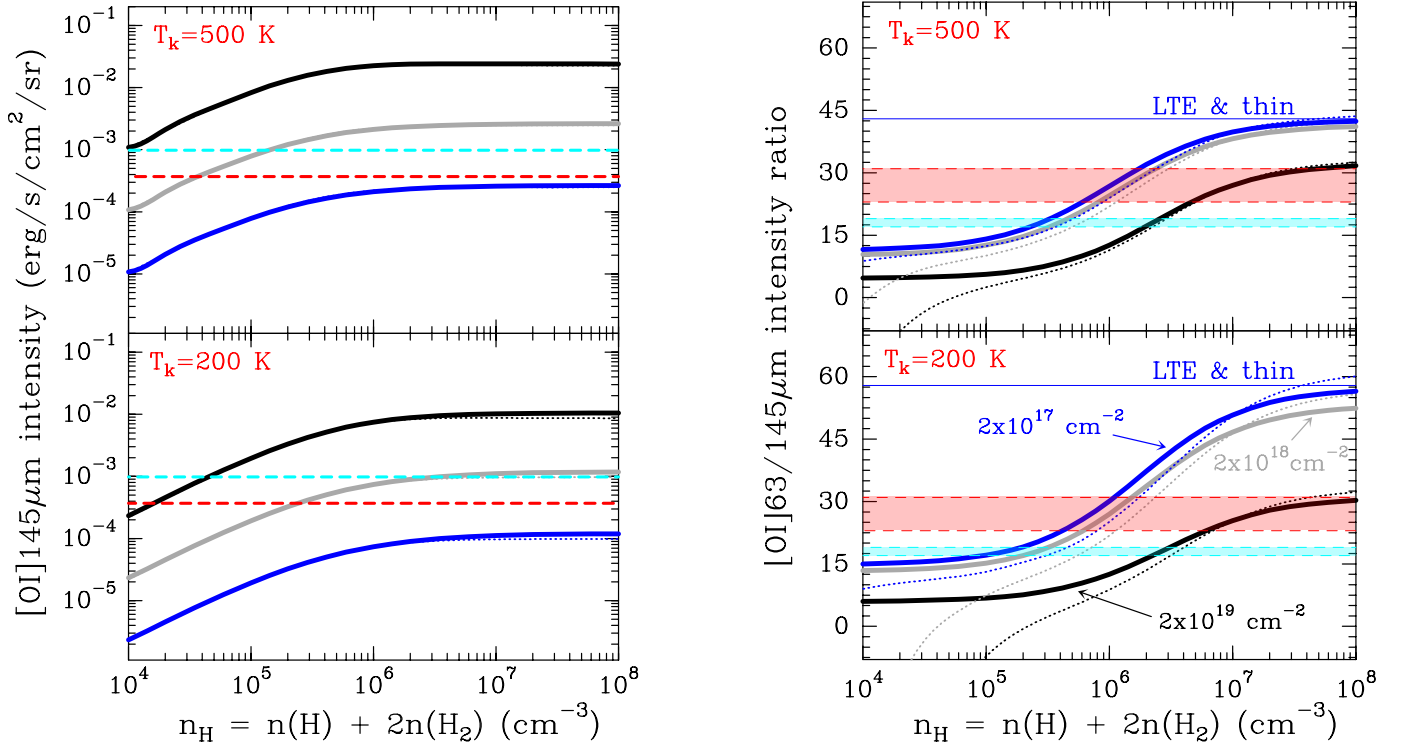


Fig. C.1. Nonlocal and non-LTE [O I] excitation and radiative transfer models: Predicted [O I] 145 μm line intensity (*left*) and [O I] 63/145 μm intensity ratio in cgs units (*right*) as a function of total gas density. The black, grey, and blue curves represent different column densities of atomic oxygen. Dotted curves represent models with external FIR illumination (see text). In the left panels, the red and cyan dashed lines show the [O I] 145 μm intensities measured toward Peak 1 in the red- and blue-shifted wings, respectively. In the right panels, the red and cyan dashed colored areas show the intensity ratios (with errors) measured toward Peak 1 in the red- and blue-shifted wings, respectively (see Table 1).

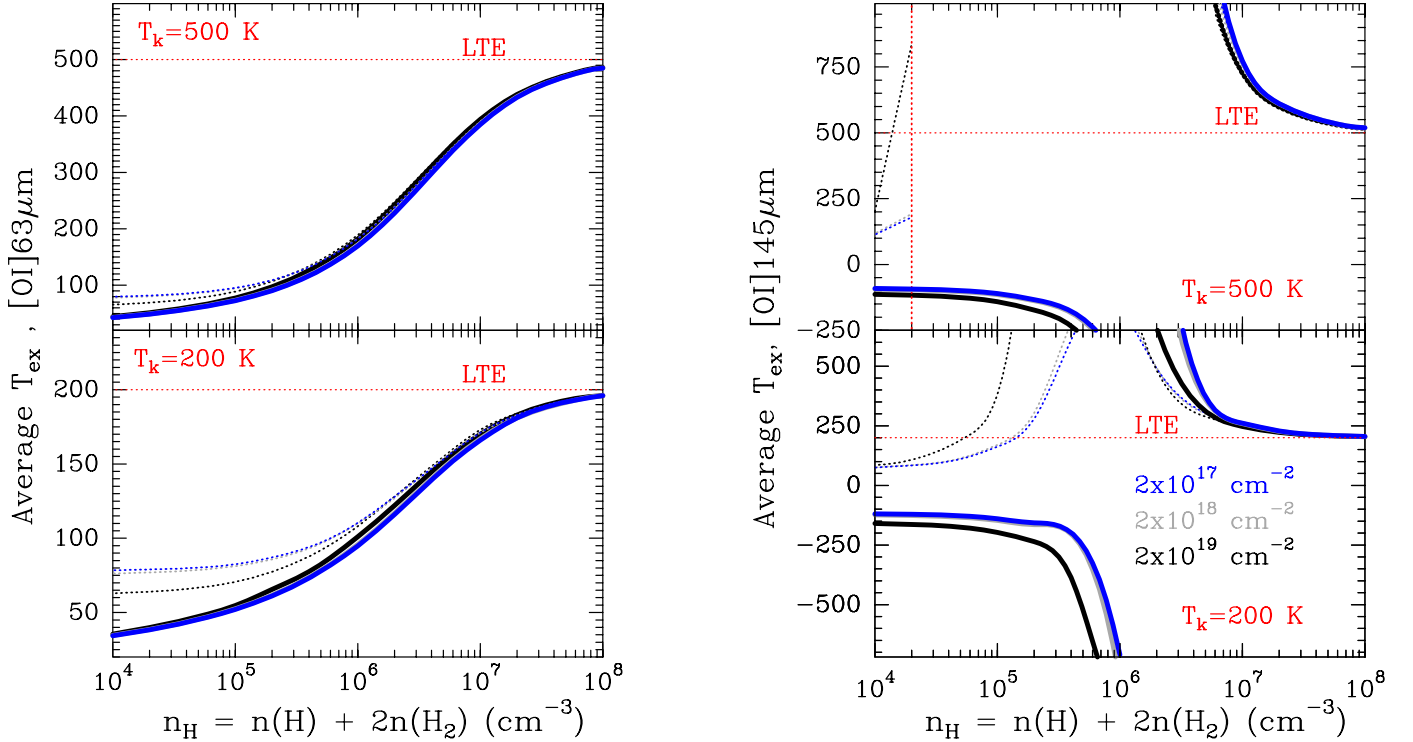


Fig. C.2. Average excitation temperature of the [O I] 63 μm and [O I] 145 μm lines as a function of gas density for two gas temperatures, 200 and 500 K. The black, grey, and blue curves represent different column densities of atomic oxygen, indicated in the right panel. Dotted curves represent models with external FIR illumination (see text). The increase in the [O I] 63 μm excitation temperature at low densities reflects the role of FIR pumping by a modified black body at $T_d = 100$ K. This effect reduces the population inversion of the transition at 145 μm at low densities.

Appendix D: Line Intensity tables

In this Appendix, we tabulate the FIR line intensities toward the Trapezium position and Peak 1, as well as the average line intensities over the entire outflow region.

Table D.1. Results of Gaussian fits to FIR lines toward the narrow [O I] 63 μm line intensity peak near the Trapezium, at an offset of (+20", -50").

Line	W (K km s ⁻¹)	I (erg s ⁻¹ cm ⁻² sr ⁻¹)	$v_{\text{LSR, peak}}$ (km s ⁻¹)	Δv (km s ⁻¹)	$T_{\text{mb, peak}}$ (K)
[O I] 63 μm	1496.9±1.0	1.638E-01	11.1±0.1	5.4±0.1	261.7
[O I] 145 μm	878.3±1.8	7.868E-03	10.5±0.1	5.0±0.1	166.0
[C II] 158 μm	1259.4±5.1	8.886E-03	10.4±0.1	5.5±0.1	215.2
CO $J = 10-9^\dagger$	348.0±0.9	5.451E-04	9.9±0.1	4.5±0.1	72.5
OH 163 μm	11.8±3.0	7.467E-05	10.8±0.4	4.0±1.8	2.8

Notes. Line intensities in a beam of 15", from maps convolved to a common angular resolution of 15", except for CO 10–9.

[†]From *Herschel*/HIFI observations of Goicoechea et al. (2019).

Table D.2. Observed FIR line intensities toward Peak 1 as a function of velocity, binned in intervals of 5 km s⁻¹ (see text and Fig. 3).

$[v_{\text{LSR}}, v_{\text{LSR}} + 5]$ (km s ⁻¹)	[O I] 63 μm ($\times 10^{-3}$ erg s ⁻¹ cm ⁻² sr ⁻¹)	[O I] 145 μm ($\times 10^{-4}$ erg s ⁻¹ cm ⁻² sr ⁻¹)	[C II] 158 μm	OH 163 μm
[-20, -15]	3.0±0.1	1.6±0.2	0.8±0.1	1.7±0.2
[-15, -10]	4.6±0.1	2.3±0.2	1.1±0.1	1.8±0.2
[-10, -5]	6.7±0.1	3.1±0.2	1.7±0.1	2.4±0.2
[-5, 0]	7.4±0.1	4.6±0.2	3.9±0.1	2.6±0.2
[0, +5]	12±1	8.7±0.2	5.5±0.1	3.0±0.2
[+5, +10]	40±1	36±1	35±1	3.5±0.2
[+10, +15]	28±1	12±1	6.4±0.1	3.5±0.2
[+15, +20]	12±1	3.9±0.2	1.2±0.1	3.3±0.2
[+20, +25]	5.5±0.1	1.8±0.2	0.8±0.1	2.9±0.2
[+25, +30]	2.8±0.1	1.0±0.2	0.5±0.1	2.1±0.2

Notes. Line intensities from maps convolved to a common angular resolution of 15".

Table D.3. Observed FIR line intensities in Orion's BN/KL outflow as a function of velocity, binned in intervals of 5 km s⁻¹, and averaged over an area of 100"×80" (see text and Fig. 3).

$[v_{\text{LSR}}, v_{\text{LSR}} + 5]$ (km s ⁻¹)	[O I] 63 μm ($\times 10^{-3}$ erg s ⁻¹ cm ⁻² sr ⁻¹)	[O I] 145 μm ($\times 10^{-4}$ erg s ⁻¹ cm ⁻² sr ⁻¹)	[C II] 158 μm	OH 163 μm
[-20, -15]	0.5±0.1	0.1±0.1	0.2±0.1	0.3±0.1
[-15, -10]	0.9±0.1	0.3±0.1	0.3±0.1	0.5±0.1
[-10, -5]	1.5±0.1	0.6±0.1	0.8±0.1	0.6±0.1
[-5, 0]	1.9±0.1	1.2±0.1	1.9±0.1	0.8±0.1
[0, +5]	4.2±0.1	3.2±0.1	4.6±0.1	1.1±0.1
[+5, +10]	35±1	28±1	31±1	1.6±0.1
[+10, +15]	25±1	11±1	14±1	1.8±0.1
[+15, +20]	5.0±0.1	1.6±0.1	1.3±0.1	1.6±0.1
[+20, +25]	1.9±0.1	0.5±0.1	0.5±0.1	1.2±0.1

Notes. Line intensities in a beam of 15", from maps convolved to a common angular resolution of 15".